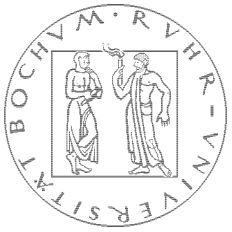

Ruhr University Bochum
Lehrstuhl für Technische Mechanik

Preprint 05-2005

Modeling strong discontinuities at finite strains – A novel numerical implementation

J. Mosler

This is a preprint of an article accepted by *Computer Methods in Applied Mechanics and Engineering*

Modeling strong discontinuities at finite strains – A novel numerical implementation

J. Mosler

Lehrstuhl für Technische Mechanik
Ruhr University Bochum
Universitätsstr. 150,D-44780 Bochum, Germany
E-Mail: mosler@tm.bi.ruhr-uni-bochum.de
URL: www.tm.bi.ruhr-uni-bochum.de/mosler

SUMMARY

In this paper, a finite element formulation suitable for the modeling of locally embedded strong discontinuities at finite strains is presented. Following the Enhanced Assumed Strain concept (EAS), the proposed numerical model is based on an additive decomposition of the displacement gradient into a conforming and an enhanced part. The enhanced part is associated with the final failure kinematics of solids which are approximated by means of a discontinuous displacement field (strong discontinuities). Referring to the displacement jump, no special assumption, such as purely mode-I or mode-II failure, is made. The same holds for the class of interface laws considered which govern the evolution of the displacement discontinuity in terms of the traction vector, acting at the surface of strong discontinuities. Consequently, the suggested numerical framework can be applied for a broad range of different interface laws, including damage based models. In contrast to previous works, the presented finite element formulation does not require the static condensation technique to be employed. More precisely, instead of computing the conforming part of deformation and the displacement jump simultaneously from the weak form of equilibrium and the weak form of traction continuity, the different parts of the local deformation are decomposed according to a predictor-corrector algorithm. The proposed predictor and the corrector step are formally identical to that of classical computational plasticity models. Hence, subroutines designed for standard models (continuous deformation) can be applied with only minor modifications necessary. The applicability as well as the performance of the resulting finite element formulation are demonstrated by means of a fully three-dimensional analysis of shear band formation in a bar made of a ductile material.

1 INTROCUCTION

The design concept most frequently applied in practical engineering is based on the ultimate load of the considered structure. If this characteristical value is greater than the forces acting, the structure is regarded as safe. However, this design concept is not always sufficient. For instance, the development of a car body requires the optimization of the respective crush zone. Only if the car body fails in a controlled manner, safety of the driver can be guaranteed. Despite the differences between the design concepts mentioned, they both require knowledge about the structural response up to the ultimate load or even up to the complete failure.

Clearly, since the mechanical problems of this kind are often very complex, numerical models are necessary. However, in the vicinity of the ultimate load and beyond, the structure is frequently characterized by strain softening. As a consequence, numerical analyses based on

standard (local) continuum models show the well-known pathological mesh-dependence, cf. [1, 2]. Furthermore, in typical applications, the width of the zones associated with localized deformations is several orders of magnitude smaller than the characteristic diameter of the structure considered. Thus, the application of enhanced continuum models, such as non-local theories [3, 4] or gradient enhanced models [5, 6] (which involve a length scale related to the failure process) for the numerical analysis of a structural component, requires sufficiently fine resolution of the localization zone; the computational cost of which may be prohibitive even if adaptive techniques are used.

One class of models which avoids the mesh dependency of the results computed numerically and accounts for the multiscale character of the underlying physical problem, is represented by the so-called Strong Discontinuity Approach (SDA) [7, 8], see also [9, 10]. In this concept, the highly localized deformations are approximated by means of discontinuous displacement fields (strong discontinuities). In contrast to interface elements [11, 12], the discontinuity is allowed to cross through solid finite elements. With the exception of the earliest published works [9, 10], the SDA is based on the Enhanced Assumed Strain concept [13, 14]. That is, only the strains induced by the discontinuous displacement field appear explicitly in the respective formulation, cf. [8, 15]. However, other promising techniques which truly model a displacement discontinuity such as the Extended Finite Element Method [16, 17] are also evolving. According to [7, 18], the kinematics associated with strong discontinuities induce a discrete constitutive model. That is, in contrast to classical continuum theories, the material response is governed by a traction separation law connecting the displacement jump to the traction vector acting at the surface of strong discontinuities. Clearly, the by now classical fictitious crack model as suggested by HILLERBORG ET AL. [19] (see also [20]) falls into the range of these traction separation laws.

Nowadays, the geometrically linearized SDA is relatively well developed. For a review article see [21]. Recently, this author proposed an efficient algorithmic framework for the numerical implementation of locally embedded strong discontinuities, cf. [22]. The fully three-dimensional finite element formulation as presented in the work cited is not restricted to any specific type of finite elements and holds for a broad range of different traction separation laws.

However, it is well known that geometrical nonlinearities affect considerably the process of strain localization. More precisely, finite deformation effects do not only influence the time of bifurcation of a homogeneously distributed strain field into a highly localized one, but also the corresponding failure mode, cf. [23]. Additionally, in many engineering applications, the response of the considered structure depends crucially on geometrical nonlinearities such as buckling. For instance, energy absorption in composite materials cannot be modeled adequately with linearized kinematics, cf. [24]. In summary, neglecting finite deformation effects can lead to an overestimation of the ultimate load of the structural component analyzed. Hence, it is reasonable to embed the SDA into a fully geometrically nonlinear framework.

The extension of the linearized kinematics of the SDA to finite strains was given by ARMERO & GARIKIPATI, cf. [25, 26]. In these references, the authors proposed a SCHMID-type traction separation law connecting the relative shear sliding displacement to the tangential component of the traction vector acting at the surface of strong discontinuities. The finite element model presented in the cited works was restricted to the two-dimensional case and based on a solution strategy almost identical to that of the EAS concept, cf. [14, 27]. In contrast to ARMERO & GARIKIPATI [25, 26], some authors approximate the displacement discontinuity by means of a ramp function. This leads to so-called regularized strong discontinuities, cf. [12, 28–30]. Since in this case, the deformation gradient is still bounded (in the sense of the operator norm), standard continuum models can be applied. However, this approximation will not be considered throughout the rest of the present paper. The finite element model which will be described in

the following sections is based directly on a traction separation law. The ideas presented by ARMERO & GARIKIPATI [25, 26] were further elaborated in [31] in which ARMERO proposed a framework to embed a localized dissipative mechanism, that is, a traction separation law, into a large scale problem, i.e. a continuous deformation. By assuming the postulate of maximum dissipation, ARMERO derived the evolution laws of the model. Restricting to linearized kinematics, a similar concept has been presented in [32, 33].

The implementations of the geometrically nonlinear SDA based finite element formulations, which have been cited so far, are almost identical to that of the EAS concept. That is, the degrees of freedom characterizing the continuous, i.e. conforming, displacement field and those associated with the displacement jump are computed simultaneously from the weak form of equilibrium and the L_2 orthogonality condition, cf. [12, 25, 28–31, 34, 35]. The resulting stiffness matrix is computed by applying the static condensation technique. As an alternative, BORJA [36] proposed a SDA based model completely avoiding the use of this technique. For the case of infinitesimal deformations, this approach was presented by BORJA and MOSLER & MESCHKE published in [37–39]. In contrast to the works [12, 25, 28–31, 34, 35], BORJA followed the ideas in [37–39] and eliminated the additional degrees of freedom corresponding to the displacement jump on the material point level. That is, the rate of the amplitude of the displacement jump was interpreted as a plastic multiplier.

In the present paper, a novel numerical implementation of locally embedded strong discontinuities is suggested. In line with [36–39], the displacement jump is condensed out at the material point level. However, in contrast to BORJA [36], no specific assumption concerning the traction separation law and the evolution equations of the displacement jump is made. That is, the new numerical implementation here proposed, holds for a broad range of different constitutive interface models. Additionally, the finite element formulation presented is embedded into a fully three-dimensional framework. To the best knowledge of the author, with the exception of the work [34] which is based on a specific damage-type traction separation law and the static condensation technique, only two-dimensional geometrically nonlinear finite element formulations can be found in the literature. In contrast to previous works on the SDA, the proposed finite element formulation is based on a return-mapping algorithm similar to that of standard plasticity theory. That is, the conforming part of deformation and the part resulting from the displacement discontinuity are computed according to a predictor-corrector step procedure, cf. [40, 41]. As a consequence, subroutines designed for classical (continuous displacement field) continuum models can be applied with only minor modifications necessary.

The present paper is organized as follows: Section 2 contains a summary of the kinematics induced by strong discontinuities. More precisely, the deformation map characterizing the SDA is explained. In Section 3, the constitutive equations are addressed. While Subsection 3.1 is concerned with material models corresponding to those points where the displacement field is continuous, interface laws connecting the displacement jump with the traction vector are developed in Subsection 3.2. These laws are formally identical to those of standard plasticity theory. Referring to the yield function and the evolution equations, no special assumption has to be made. Section 4 is concerned with the new algorithmic framework for the numerical implementation of locally embedded strong discontinuities at finite strains. At first, the fundamentals are discussed in Subsection 4.1. Subsequently, the solution strategy associated with an elastic loading step is addressed (Subsection 4.2). Finally, Subsection 4.3 contains the algorithmic formulation corresponding to an inelastic loading step. In Section 5, the efficiency of the resulting finite element model is investigated by means of a fully three-dimensional analysis of shear band formation in a bar made of a ductile material.

As for the notation, the symbol '$\cdot$' represents the standard simple contraction of two tensors. That is, with the first-order tensors $\boldsymbol{a}$, $\boldsymbol{b}$, the second-order tensors $\boldsymbol{A}$, $\boldsymbol{B}$ and the fourth-order

tensor $\mathbb{C}$ the identities $\boldsymbol{a}\cdot\boldsymbol{b} = a_i\, b_i$ and $[\boldsymbol{A}\cdot\boldsymbol{b}]_i = A_{ij}\, b_j$ hold (EINSTEIN summation convention is used). Furthermore, the well-known double contraction, i.e. $\boldsymbol{A} : \boldsymbol{B} = A_{ij}B_{ij}$ and $[\mathbb{C} : \boldsymbol{\varepsilon}]_{ij} = \mathbb{C}_{ijkl}\, \varepsilon_{kl}$, is used throughout the paper. However, different types of contraction are sometimes necessary. For that purpose, index notation is used in many cases. Alternatively, the notations $\overset{(i)}{\cdot}$ and $\overset{(i)}{:}$ are applied. Here, i indicates the first component of the tensor on the right hand side of $\overset{(i)}{\cdot}$ or $\overset{(i)}{:}$ over which the summation has to be performed. That is, $[\boldsymbol{a} \overset{(2)}{\cdot} \mathbb{C}]_{jkl} = a_i\, \mathbb{C}_{jikl}$ and $[\boldsymbol{A} \overset{(2)}{:} \mathbb{C}]_{il} = A_{jk}\, \mathbb{C}_{ijkl}$. Clearly, for $i = 1$ the standard contractions are obtained.

Although only the canonical metric of $\mathbb{R}^n$ is chosen in this paper, the notations *pull-back* and *push-forward* are sometimes used. It is obvious that they are defined in the standard manner, cf. [40].

2 KINEMATICS INDUCED BY STRONG DISCONTINUITIES

This section contains the fundamentals of the kinematics induced by strong discontinuities. For further details, refer to [7, 21, 26, 31, 42].

In what follows, a domain $\Omega \subset \mathbb{R}^3$, that is, an open bounded and connected set, is assumed to be cut into two parts Ω^- and Ω^+. In this connection, the cut denoted as $\partial_{\mathrm{s}}\Omega$ which defines the subsets Ω^- and Ω^+ is postulated to be piecewise a hyperplane of class $\mathcal{C}^1$. This condition guarantees a well-defined normal vector field $\boldsymbol{N}$ (piecewise). From a physical point of view, the submanifold $\partial_{\mathrm{s}}\Omega$ may represent a crack surface or a slip plane with respect to the undeformed configuration. It is obvious that the subsets Ω^- and Ω^+ are well defined, if $\partial_{\mathrm{s}}\Omega$ is connected. For instance, using $\partial_{\mathrm{s}}\Omega \subset \overline{\Omega^+}$ (the hyperplane is part of the closure of Ω^+), together with the fact that $\overline{\Omega^+}$ is connected, Ω^+ is defined uniquely by

$$\Omega^+ = \left\{ \boldsymbol{X} \in \Omega \mid \exists \boldsymbol{X}_0 = \boldsymbol{X}_0(\boldsymbol{X}) \in \partial_{\mathrm{s}}\Omega, \text{ with } (\boldsymbol{X} - \boldsymbol{X}_0)\cdot \boldsymbol{N}|_{\boldsymbol{X}_0} > 0 \right\}. \tag{1}$$

In the case of a planar hyperplane $\partial_{\mathrm{s}}\Omega$, which will be considered in the finite element formulation presented in Section 4, Equation (1) results in

$$\Omega^+ = \left\{ \boldsymbol{X} \in \Omega \;\middle|\; (\boldsymbol{X} - \boldsymbol{X}_0)\cdot \boldsymbol{N}|_{\boldsymbol{X}_0} > 0 \right\}, \quad \forall \boldsymbol{X}_0 \in \partial_{\mathrm{s}}\Omega. \tag{2}$$

That is, in contrast to Equation (1), the scalar product in Equation (2) can be computed for an arbitrary point $\boldsymbol{X}_0 \in \partial_{\mathrm{s}}\Omega$.

Next, a discontinuous deformation mapping $\boldsymbol{\varphi}$ is considered. This mapping connects each point $\boldsymbol{X}$ in the reference configuration Ω to the corresponding point $\boldsymbol{x}$ in the current placement $\boldsymbol{\varphi}(\Omega)$. Clearly, since Ω is assumed as connected and $\boldsymbol{\varphi} = \mathrm{id}_\Omega + \boldsymbol{u}$, a discontinuous deformation mapping is equivalent to a discontinuous displacement field $\boldsymbol{u}$. In what follows, a displacement mapping of the type

$$\boldsymbol{u}|_{\Omega^\pm} \in \mathcal{C}^\infty(\Omega^\pm, \mathbb{R}^3), \qquad \Omega^\pm := \Omega^+ \cup \Omega^- \tag{3}$$

is considered. That is, $\boldsymbol{u}$ may be discontinuous at $\partial_{\mathrm{s}}\Omega$ while it is smooth on $\Omega^\pm$. This restriction is reasonable, since the finite element model as proposed in Section 4 is based on a polynomial approximation of the displacement field $\boldsymbol{u}|_{\Omega^\pm}$. Applying condition (3), the left hand limit $\boldsymbol{u}^-(\boldsymbol{X}_0)$ and the right hand limit $\boldsymbol{u}^+(\boldsymbol{X}_0)$ of the displacement mapping $\boldsymbol{u} : \Omega \to \mathbb{R}^3$ at $\boldsymbol{X}_0 \in \partial_{\mathrm{s}}\Omega$ are obtained as

$$\boldsymbol{u}^\pm(\boldsymbol{X}_0) := \lim_{n\to\infty} \boldsymbol{u}(\boldsymbol{X}_n^\pm), \quad (\boldsymbol{X}_n^\pm)_{n\in\mathbb{N}} \in (\Omega^\pm)^{\mathbb{N}}, \quad \boldsymbol{X}_n^\pm \to \boldsymbol{X}_0 \; (n \to \infty). \tag{4}$$

Hence, the discontinuity of $\boldsymbol{u}$ at $\boldsymbol{X}_0$ is computed as

$$[\![\boldsymbol{u}(\boldsymbol{X}_0)]\!] := \boldsymbol{u}^+(\boldsymbol{X}_0) - \boldsymbol{u}^-(\boldsymbol{X}_0) \quad \forall \boldsymbol{X}_0 \in \partial_{\mathrm{s}}\Omega. \tag{5}$$

Following [7, 8, 15], the finite element formulation presented in Section 4 is based on a displacement field of the type

$$\boldsymbol{u} = \hat{\boldsymbol{u}} + [\![\boldsymbol{u}]\!]\ (H_{\mathrm{s}} - \varphi), \quad \text{with} \quad \hat{\boldsymbol{u}} \in \mathcal{C}^\infty(\Omega, \mathbb{R}^3),\ \varphi \in \mathcal{C}^\infty(\Omega, \mathbb{R}) \tag{6}$$

where $H_{\mathrm{s}} : \Omega \to \{0; 1\}$ denotes the HEAVISIDE function with respect to the singular surface $\partial_{\mathrm{s}}\Omega$ and φ represents a smooth ramp function necessary to prescribe the boundary conditions in terms of $\hat{\boldsymbol{u}}$ (see [15]). It is obvious that $\boldsymbol{u}$ belongs to the space of bounded deformations as introduced in [43, 44]. Referring to the finite element method as proposed in Section 4, φ is designed by the standard interpolation functions N_i associated with node i as

$$\varphi = \sum_{i=1}^{n_{\overline{\Omega^+}}} N_i. \tag{7}$$

For further details, refer to [8, 21]. In Equation (7), the summation is performed over all shape functions associated with a node belonging to $\overline{\Omega^+}$. By applying the generalized derivative $D(\bullet)$ to Equation (6), the deformation gradient is computed as

$$\boldsymbol{F} = \boldsymbol{1} + \frac{\partial \hat{\boldsymbol{u}}}{\partial \boldsymbol{X}} + \frac{\partial\, [\![\boldsymbol{u}]\!]}{\partial \boldsymbol{X}}\ (H_{\mathrm{s}} - \varphi) + [\![\boldsymbol{u}]\!] \otimes \boldsymbol{N}\ \delta_{\mathrm{s}} - [\![\boldsymbol{u}]\!] \otimes \frac{\partial \varphi}{\partial \boldsymbol{X}} \tag{8}$$

where the identity $DH_{\mathrm{s}} = \boldsymbol{N}\ \delta_{\mathrm{s}}$ connecting the HEAVISIDE function and the DIRAC-delta distribution has been used, cf. [45, 46]. Evidently, Equation (8) has to be interpreted in a distributional sense.

The finite element formulation as presented in Section 4 is based on the Enhanced Assumed Strain concept (EAS), cf. [13, 14, 27]. Consequently, the enhanced part of the deformation gradient is modeled in an incompatible fashion. If only the displacement field $\hat{\boldsymbol{u}}$ is approximated globally (conforming), that is,

$$\hat{\boldsymbol{u}} = \sum_{i=1}^{n_{\mathrm{node}}} N_i\ \hat{\boldsymbol{u}}_i^{\mathrm{e}}, \tag{9}$$

with the nodal displacements $\hat{\boldsymbol{u}}_i^{\mathrm{e}}$ at node i, the deformation gradient (8) can be decomposed additively into a conforming part

$$\hat{\boldsymbol{F}} := \boldsymbol{1} + \mathrm{GRAD}\hat{\boldsymbol{u}}, \qquad \mathrm{GRAD}\hat{\boldsymbol{u}} := \frac{\partial \hat{\boldsymbol{u}}}{\partial \boldsymbol{X}} \tag{10}$$

and an incompatible enhanced displacement gradient

$$\boldsymbol{H} = \frac{\partial\, [\![\boldsymbol{u}]\!]}{\partial \boldsymbol{X}}\ (H_{\mathrm{s}} - \varphi) + [\![\boldsymbol{u}]\!] \otimes \boldsymbol{N}\ \delta_{\mathrm{s}} - [\![\boldsymbol{u}]\!] \otimes \frac{\partial \varphi}{\partial \boldsymbol{X}}. \tag{11}$$

Since $\boldsymbol{H}$ needs not to represent the derivative of a conforming discontinuous deformation field, it is admissible to neglect the gradient of the displacement discontinuity, i.e. $\partial\, [\![\boldsymbol{u}]\!] / \partial \boldsymbol{X} = \boldsymbol{0}$ and to consider a deformation gradient of the type

$$\boldsymbol{F} = \boldsymbol{1} + \frac{\partial \hat{\boldsymbol{u}}}{\partial \boldsymbol{X}} + [\![\boldsymbol{u}]\!] \otimes \boldsymbol{N}\ \delta_{\mathrm{s}} - [\![\boldsymbol{u}]\!] \otimes \frac{\partial \varphi}{\partial \boldsymbol{X}}. \tag{12}$$

The deformation gradient according to Equation (12) will be used in the finite element model presented in Section 4. For a detailed analysis concerning the kinematics, refer to [21].

The additive decomposition (12) of the deformation gradient is not well-suited for the development of constitutive equations. Following [25, 26], Equation (12) is rewritten into a multiplicative decomposition as

$$\boldsymbol{F} = \bar{\boldsymbol{F}} \cdot \tilde{\boldsymbol{F}}, \qquad \text{with} \qquad \begin{array}{rcll} \bar{\boldsymbol{F}} & = & \boldsymbol{1} + \text{GRAD}\hat{\boldsymbol{u}} - [\![\boldsymbol{u}]\!] \otimes \text{GRAD}\varphi & \\ \tilde{\boldsymbol{F}} & = & \boldsymbol{1} + \boldsymbol{J} \otimes \boldsymbol{N}\, \delta_{\text{s}}, & \boldsymbol{J} := \bar{\boldsymbol{F}}^{-1} \cdot [\![\boldsymbol{u}]\!]\,. \end{array} \tag{13}$$

As a consequence, $\bar{\boldsymbol{F}}$ represents the regularly distributed part of the deformation gradient while $\tilde{\boldsymbol{F}}$ is associated with the singular distribution resulting from the generalized derivative of the displacement jump. In Equation (13), $\boldsymbol{J}$ denotes the material counterpart of the displacement discontinuity. That is, in a differential geometry framework, $\boldsymbol{J}$ is the pull-back of $[\![\boldsymbol{u}]\!]$ with respect to the mapping represented by $\bar{\boldsymbol{F}}$. Therefore, $\boldsymbol{J}$ can be interpreted as a vector on the intermediate configuration implied by the multiplicative decomposition $(13)_1$. However, since

$$\boldsymbol{F}|_{\Omega^{\pm}} = \bar{\boldsymbol{F}}|_{\Omega^{\pm}}, \tag{14}$$

the pull-back of tensors (with $\bar{\boldsymbol{F}}$) defined on $\boldsymbol{\varphi}(\Omega^{\pm})$ leads to objects on the undeformed configuration. More precisely, the multiplicative decomposition $(13)_1$ holds only for $\boldsymbol{X}_0 \in \partial_{\text{s}}\Omega$. For $\boldsymbol{X} \in \Omega^{\pm}$ it reduces to $\boldsymbol{F} = \bar{\boldsymbol{F}}$.

Analogously to standard multiplicative plasticity theory, the spatial velocity gradient $\boldsymbol{l} := \dot{\boldsymbol{F}} \cdot \boldsymbol{F}^{-1}$ is computed as

$$\boldsymbol{l} = \bar{\boldsymbol{l}} + \tilde{\boldsymbol{l}}, \qquad \text{with} \qquad \begin{array}{rcl} \bar{\boldsymbol{l}} & = & \dot{\bar{\boldsymbol{F}}} \cdot \bar{\boldsymbol{F}}^{-1} \\ \tilde{\boldsymbol{l}} & = & \bar{\boldsymbol{F}} \cdot \dot{\tilde{\boldsymbol{F}}} \cdot \tilde{\boldsymbol{F}}^{-1} \cdot \bar{\boldsymbol{F}}^{-1}. \end{array} \tag{15}$$

Here and henceforth, the superposed dot represents the material time derivative. According to Equation (15), $\boldsymbol{l}$ is decomposed additively. It consists of a part $\bar{\boldsymbol{l}}$, associated with the continuous deformation mapping and a second term $\tilde{\boldsymbol{l}}$, resulting from the rate of the displacement discontinuity. Since $\bar{\boldsymbol{F}}$ is regularly distributed, $\bar{\boldsymbol{l}}$ can be computed in standard manner. However, to obtain $\tilde{\boldsymbol{l}}$, an inversion of a singular distribution is necessary. To the best knowledge of the author, $\tilde{\boldsymbol{l}}$ was computed in [25, 26] for the first time. For that purpose, $\tilde{\boldsymbol{F}}$ was interpreted as a linear mapping between two vector spaces. Alternatively, it is possible to approximate the DIRAC-delta function by using an h-sequence, that is,

$$\delta_{\text{s}}^h := \frac{\chi_{\partial_{\text{s}}\Omega}}{h}, \quad \delta_{\text{s}}^h \to \delta_{\text{s}} \quad (h \to \infty), \tag{16}$$

applying the well-known SHERMAN-MORRISON formula and computing the limiting value, i.e. $h \to \infty$, cf. [28]. Both procedures result in

$$\tilde{\boldsymbol{l}} = \mathcal{L}_{\nu}\, [\![\boldsymbol{u}]\!] \otimes \boldsymbol{N} \cdot \bar{\boldsymbol{F}}^{-1}\, \delta_{\text{s}} \tag{17}$$

where $\mathcal{L}_{\nu}\, [\![\boldsymbol{u}]\!]$ represents a LIE-type derivative according to

$$\mathcal{L}_{\nu}\, [\![\boldsymbol{u}]\!] = \bar{\boldsymbol{F}} \cdot \frac{\partial}{\partial t} \left\{ \bar{\boldsymbol{F}}^{-1} \cdot [\![\boldsymbol{u}]\!] \right\} = [\![\dot{\boldsymbol{u}}]\!] + \bar{\boldsymbol{l}} \cdot [\![\boldsymbol{u}]\!]\,. \tag{18}$$

In Equation (16), $\chi_{\partial_{\text{s}}\Omega}$ denotes the indicating function of the subset $\partial_{\text{s}}\Omega$.

Remark 1. *The kinematics, as well as the finite element implementation proposed in Subsection 4, are based on only one localization surface within the respective body Ω (the finite element). For the case of multiple strong discontinuities, see [21, 47].*

Remark 2. *Since in what follows, an evolution equation for $\boldsymbol{J}$ will be applied, $\tilde{\boldsymbol{F}}$ can be computed. As a consequence, the intermediate configuration induced by the multiplicative decomposition (13) of the deformation gradient is defined uniquely.*

3 CONSTITUTIVE EQUATIONS

3.1 Constitutive Equations for $\boldsymbol{X} \in \Omega^{\pm}$

According to Section 2, $\boldsymbol{F}|_{\Omega^{\pm}}$ is regularly distributed. As a consequence, standard stress-strain relationship based continuum models can be applied. Since the main focus of the present paper is on the modeling of localized inelastic deformations, the homogeneously distributed part of deformation is assumed as purely elastic. More precisely, the existence of a stored-energy functional $\Psi_{\mathrm{reg}} = \Psi_{\mathrm{reg}}(\bar{\boldsymbol{F}})$ is postulated. Clearly, other constitutive models such as plasticity based formulations can be easily applied as well. By taking into account the principle of objectivity, the regularly distributed part of the deformation gradient enters the stored-energy function through the right CAUCHY-GREEN tensor

$$\bar{\boldsymbol{C}} := \bar{\boldsymbol{F}}^{T} \cdot \bar{\boldsymbol{F}}. \tag{19}$$

Note that the identity $\bar{\boldsymbol{C}}|_{\Omega^{\pm}} = \boldsymbol{C}|_{\Omega^{\pm}}$ holds.

Computing the stress power $\mathcal{P}$ in terms of KIRCHHOFF stresses $\boldsymbol{\tau}$ for $\boldsymbol{X} \in \Omega^{\pm}$, i.e.

$$\mathcal{P} = \boldsymbol{\tau} : \boldsymbol{l} = \boldsymbol{\tau} : \bar{\boldsymbol{l}}, \tag{20}$$

the dissipation $\mathcal{D}$ is obtained as

$$\mathcal{D} = \boldsymbol{\tau} : \bar{\boldsymbol{d}} - \partial_{\bar{\boldsymbol{C}}} \Psi_{\mathrm{reg}} : \dot{\bar{\boldsymbol{C}}}, \quad \text{with} \quad \bar{\boldsymbol{d}} := \bar{\boldsymbol{l}}^{\mathrm{sym}}. \tag{21}$$

Since the material response in $\Omega^{\pm}$ has been postulated to be purely elastic, $\mathcal{D} = 0$. As a consequence, inserting the identity $\dot{\bar{\boldsymbol{C}}} = 2\ \bar{\boldsymbol{F}}^{T} \cdot \bar{\boldsymbol{d}} \cdot \bar{\boldsymbol{F}}$, yields

$$\boldsymbol{\tau} = 2\ \bar{\boldsymbol{F}} \cdot \partial_{\bar{\boldsymbol{C}}} \Psi_{\mathrm{reg}} \cdot \bar{\boldsymbol{F}}^{T} \qquad \text{and} \qquad \boldsymbol{S} = 2\ \partial_{\bar{\boldsymbol{C}}} \Psi_{\mathrm{reg}}, \tag{22}$$

with $\boldsymbol{S}$ denoting the second PIOLA-KIRCHHOFF stress tensor, see Remark 3.

In the numerical analyses presented in Section 5, an energy functional Ψ_{reg} of the type

$$\Psi_{\mathrm{reg}}(\bar{\boldsymbol{C}}) = \lambda\ \frac{J^2 - 1}{4} - \left(\frac{\lambda}{2} + \mu\right)\ \ln J + \frac{1}{2}\ \mu\ \left(\mathrm{tr}\bar{\boldsymbol{C}} - 3\right) \tag{23}$$

is adopted where J, tr, λ, μ denote the determinant of the deformation gradient $\bar{\boldsymbol{F}}$, the trace operation and the LAMÉ constants, respectively. For further details concerning this polyconvex stored-energy functional, refer to [48].

Remark 3. *Since the stress tensors are only defined for $\boldsymbol{X} \in \Omega^{\pm}$, and for those points the identity $\bar{\boldsymbol{F}}|_{\Omega^{\pm}} = \boldsymbol{F}|_{\Omega^{\pm}}$ holds, the bar over the second* PIOLA-KIRCHHOFF *stress tensor $\boldsymbol{S}$ is omitted.*

3.2 Constitutive Equations for $\boldsymbol{X} \in \partial_{\mathrm{s}}\Omega$: Traction separation laws

Postulating a purely elastic response in $\Omega^{\pm}$, inelastic deformations are governed by the respective material model associated with points belonging to $\partial_{\mathrm{s}}\Omega$. Since in general, the constitutive relationships for $\boldsymbol{X} \in \Omega^{\pm}$ and those for $\boldsymbol{X} \in \partial_{\mathrm{s}}\Omega$ are completely independent of each other, it is reasonable to decompose the stored-energy functional into two parts, namely one characterizing the hyperelastic material response in $\Omega^{\pm}$ and an additional term which reflects the localized deformation adequately. As a consequence, a stored-energy functional of the type

$$\Psi(\bar{\boldsymbol{C}}, \boldsymbol{J}, \boldsymbol{\alpha}) = \Psi_{\mathrm{reg}}(\bar{\boldsymbol{C}}) + \Psi_{\mathrm{sing}}(\boldsymbol{J}, \boldsymbol{\alpha})\ \delta_{\mathrm{s}} \tag{24}$$

represents a suitable choice. According to Equation (24), the localized nature of the deformation is reflected by the singular DIRAC-delta function which is multiplied by the functional Ψ_{sing} depending on the material displacement jump $\boldsymbol{J}$ and some internal displacement-like variables $\boldsymbol{\alpha}$ describing inelastic phenomena such as hardening or softening. A similar decomposition as that in Equation (24) was postulated by several authors, cf. [15, 21, 30, 32, 49, 50]. It should be noted that an additive decomposition of the functional Ψ according to Equation (24) is also frequently applied in the context of standard ($\boldsymbol{\varphi}$ is continuous) continuum models, cf. [41, 51, 52].

Next, attention is restricted to purely inelastic localized deformations. That is, the displacement jump $\boldsymbol{J}$ corresponds to fully inelastic deformations. In this case, $\boldsymbol{J}$ can also be interpreted as a displacement-like internal variable. Hence, $\Psi_{\text{sing}}(\boldsymbol{J}, \boldsymbol{\alpha})$ reduces to $\Psi_{\text{sing}}(\boldsymbol{\alpha}(\boldsymbol{J}))$. Evidently, a decomposition of $\boldsymbol{J}$ into an elastic and an inelastic part can be easily applied as well, cf. [31, 32].

So far, the mechanical problem describing the material response in $\Omega^{\pm}$ and that corresponding to $\boldsymbol{X} \in \partial_{\text{s}}\Omega$ are uncoupled. The coupling is provided by the condition of continuity of the traction vector $\boldsymbol{T} := \boldsymbol{P} \cdot \boldsymbol{N}$ where $\boldsymbol{P}$ denotes the first PIOLA-KIRCHHOFF stress tensor:

$$\boldsymbol{T}^{-}(\boldsymbol{X}_0) = \boldsymbol{T}^{+}(\boldsymbol{X}_0) = \boldsymbol{T}(\boldsymbol{X}_0), \quad \boldsymbol{X}_0 \in \partial_{\text{s}}\Omega, \tag{25}$$

with $\boldsymbol{T}^{\pm}$ denoting the left hand and the right hand limits of the traction vector $\boldsymbol{T}$ according to Equation (4). This canonical condition follows from the extension of the principal of virtual work to continua with internal surfaces $\partial_{\text{s}}\Omega$, if the space of admissible test functions is chosen as that spanned by the displacement field (6), i.e. GALERKIN-type. For further details, refer to [8]. Condition (25) allows to compute the stress vector $\boldsymbol{T}(\boldsymbol{X}_0)$ by means of the hyperelastic material law associated with $\boldsymbol{X} \in \Omega^{\pm}$.

Now, the dissipation $\mathcal{D}$ in $\partial_{\text{s}}\Omega$ can be calculated. Combining Condition (25) and the hyperelastic law (22), together with the spatial velocity gradient (15), $\mathcal{D}$ is obtained as

$$\mathcal{D} = \boldsymbol{\tau} : \boldsymbol{l} - \dot{\Psi} = \left[\left(\boldsymbol{\tau} \cdot \bar{\boldsymbol{F}}^{-T} \cdot \boldsymbol{N} \right) \cdot \mathcal{L}_{\nu} [\![\boldsymbol{u}]\!] + \boldsymbol{q} \cdot \dot{\boldsymbol{\alpha}} \right] \delta_{\text{s}} \geq 0. \tag{26}$$

In Equation (26), the internal stress-like variables $\boldsymbol{q} := -\partial_{\boldsymbol{\alpha}} \Psi_{\text{sing}}$ conjugated to $\boldsymbol{\alpha}$ have been introduced. Hence, the scalar product $\boldsymbol{q} \cdot \dot{\boldsymbol{\alpha}}$ depends on the order of the tensor $\boldsymbol{\alpha}$. Alternatively, the dissipation can be rewritten as

$$\mathcal{D} = \left[\left(\bar{\boldsymbol{C}} \cdot \boldsymbol{S} \cdot \boldsymbol{N} \right) \cdot \dot{\boldsymbol{J}} + \boldsymbol{q} \cdot \dot{\boldsymbol{\alpha}} \right] \delta_{\text{s}} \geq 0. \tag{27}$$

Note that Inequality (27) is formally identical to its counterpart of standard multiplicative plasticity. To show this equivalence more explicitly, the pull-back (with respect to the intermediate configuration) of $\tilde{\boldsymbol{l}}$ resulting in

$$\tilde{\boldsymbol{L}} = \dot{\boldsymbol{J}} \otimes \boldsymbol{N} \, \delta_{\text{s}} \tag{28}$$

is introduced. With Equation (28), the dissipation yields

$$\mathcal{D} = \left(\bar{\boldsymbol{C}} \cdot \boldsymbol{S} \right) : \tilde{\boldsymbol{L}} + \boldsymbol{q} \cdot \dot{\boldsymbol{\alpha}} \, \delta_{\text{s}} \geq 0. \tag{29}$$

Fully analogously to standard continuum models, the dissipation which is now computed with respect to the intermediate configuration depends on the MANDEL stresses $\bar{\boldsymbol{C}} \cdot \boldsymbol{S}$. Note that $\boldsymbol{\alpha} = \boldsymbol{\alpha}(\boldsymbol{J})$. Hence, $\boldsymbol{\alpha}$ and $\boldsymbol{q}$ are also defined on the intermediate configuration and $\dot{\boldsymbol{\alpha}}$ represents an objective time derivative.

The evolution equations, that is, $\dot{\boldsymbol{J}}$ and $\dot{\boldsymbol{\alpha}}$, are computed from the postulate of maximum dissipation under the constraint imposed by the condition of traction continuity. Following [21, 22] and using the positive definiteness of a norm $||\bullet||$, the constraint (25) is rewritten as

$$\phi := ||\boldsymbol{T}^{+}(\boldsymbol{X}_0) - \boldsymbol{T}(\boldsymbol{X}_0)|| = 0. \tag{30}$$

Alternatively, a pull-back yields

$$\phi := ||\bar{\boldsymbol{T}}^{+}(\boldsymbol{X}_0) - \bar{\boldsymbol{T}}(\boldsymbol{X}_0)|| = 0, \quad \text{with} \quad \bar{\boldsymbol{T}} := \bar{\boldsymbol{C}} \cdot \boldsymbol{S} \cdot \boldsymbol{N}. \tag{31}$$

Evidently, this equation is fully equivalent to the necessary condition of yielding known from standard plasticity models. By this equivalence, the definition of the space of admissible stresses

$$\mathbb{E}_{\bar{\boldsymbol{T}}} := \left\{ (\bar{\boldsymbol{T}}^{+}, \boldsymbol{q}) \in \mathbb{R}^3 \times \mathbb{R}^n \mid \phi(\bar{\boldsymbol{T}}^{+}, \boldsymbol{q}) \leq 0 \right\} \tag{32}$$

is motivated. Restricting to the geometrically linear theory, further details are addressed in [21, 22]. For the special choice, $\boldsymbol{q} = \bar{\boldsymbol{T}}(\boldsymbol{X}_0)$ and $\phi(\bar{\boldsymbol{T}}^{+}, \boldsymbol{q}) = ||\bar{\boldsymbol{T}}^{+} - \boldsymbol{q}||$, $\phi = 0$ is equivalent to the condition of traction continuity.

However, the condition $\boldsymbol{T}^{+} = \boldsymbol{T}_{\mathrm{s}} := \boldsymbol{T}|_{\partial_{\mathrm{s}}\Omega}$ has only to be enforced to compute the inelastic part of the deformation, that is, $\dot{\boldsymbol{J}}$ and $\dot{\boldsymbol{\alpha}}$. In the case of fully elastic loading, the stress response is defined uniquely by Equation (22). As a consequence, the condition of traction continuity has only to be enforced to those components of the traction vector $\bar{\boldsymbol{T}}$ which are conjugated with a non-vanishing component of the material displacement jump $\boldsymbol{J}$. Hence, $\phi(\bar{\boldsymbol{T}}^{+}, \boldsymbol{q})$ needs not necessarily to be identical to $||\bar{\boldsymbol{T}}^{+}(\boldsymbol{X}_0) - \bar{\boldsymbol{T}}(\boldsymbol{X}_0)||$. For instance, plastic deformations occurring in slip bands in ductile materials such as metals depend exclusively on the resultant of the shear components of $\bar{\boldsymbol{T}}$. Furthermore, the material response associated with metals does not differentiate between compressive or tensile loading. Hence,

$$\phi = ||\bar{\boldsymbol{T}}^{+}_{m}||_2 - q(\alpha), \quad \text{with} \quad \bar{\boldsymbol{T}}^{+}_{m} := \bar{\boldsymbol{T}}^{+} - (\bar{\boldsymbol{T}}^{+} \cdot \boldsymbol{N})\, \boldsymbol{N}. \tag{33}$$

represents a suitable choice. In the context of linearized kinematics, this yield function was proposed in [22]. It will be used in the numerical analysis presented in Section 5.

In summary, the postulate of maximum dissipation subjected to the condition of traction continuity can be written as

$$\text{compute:} \ \min_{\bar{\boldsymbol{T}}^{+}, \boldsymbol{q}, \lambda} \mathcal{L}, \quad \text{with} \quad \mathcal{L}(\bar{\boldsymbol{T}}^{+}, \boldsymbol{q}, \lambda) := -\mathcal{D} + \lambda\, \phi. \tag{34}$$

Consequently, the evolution equation are obtained as

$$\dot{\boldsymbol{J}} = \lambda\, \partial_{\bar{\boldsymbol{T}}^{+}} \phi, \qquad \dot{\boldsymbol{\alpha}} = \lambda\, \partial_{\boldsymbol{q}} \phi. \tag{35}$$

The plastic multiplier λ as introduced in Definition (34) is computed from the consistency condition $\dot{\phi} = 0$. Analogously to standard plasticity theory, the evolution laws are defined completely by means of the yield function, if the postulate of maximum dissipation is enforced. It is obvious that non-associative material models can be derived in a similar manner. For that purpose, two potentials $g = g(\bar{\boldsymbol{T}}^{+}, \boldsymbol{q})$ and $h = h(\bar{\boldsymbol{T}}^{+}, \boldsymbol{q})$ are introduced and the evolution equations are specified by

$$\dot{\boldsymbol{J}} = \lambda\, \partial_{\bar{\boldsymbol{T}}^{+}} g, \qquad \dot{\boldsymbol{\alpha}} = \lambda\, \partial_{\boldsymbol{q}} h. \tag{36}$$

For the yield function (33), the respective associative evolution equations are contained in [22].

The singular surface $\partial_{\mathrm{s}}\Omega$ has been postulated to be time invariant, i.e. $\dot{\boldsymbol{N}} = \boldsymbol{0}$. Consequently,

$$\phi(\bar{\boldsymbol{T}}^{+}, \boldsymbol{q}) = \phi^{*}(\bar{\boldsymbol{C}} \cdot \boldsymbol{S}, \boldsymbol{q}), \quad \text{with} \quad \phi^{*}(\boldsymbol{A}, \boldsymbol{b}) := \phi(\boldsymbol{A} \cdot \boldsymbol{N}, \boldsymbol{b}). \tag{37}$$

Hence, equivalently to Equation $(36)_1$, the evolution law

$$\dot{\boldsymbol{J}} \otimes \boldsymbol{N} = \lambda \, \partial_{\bar{\boldsymbol{C}} \cdot \boldsymbol{S}} g^* \tag{38}$$

can be derived. Thus, the space of admissible stresses is formulated in terms of MANDEL-stresses and the evolution law associated with inelastic deformations governs the inelastic velocity gradient $\tilde{\boldsymbol{L}}$. That is, the constitutive equations describing the localized inelastic part of the deformation are formally identical to those known from standard plasticity.

So far, the kinematics as well as the constitutive equations characterizing a discontinuous deformation mapping have been presented. However, the normal vector $\boldsymbol{N}$ defining the orientation of the localization surface $\partial_{\mathrm{s}}\Omega$ has been regarded as known. In the literature, different criteria for the prediction of the formation and the orientation of a surface at which the displacements are not continuous can be found. Most frequently, stress-based criteria or bifurcation analyses according to [7] are applied. However, other methods are suitable as well, cf. [21]. In the numerical analyses presented in Section 5, a stress-based concept will be used.

In the following sections, the condition of traction continuity will be replaced by the more general type of equations $\phi(\bar{\boldsymbol{T}}^+, \boldsymbol{q})$ or $\phi^*(\bar{\boldsymbol{C}} \cdot \boldsymbol{S}, \boldsymbol{q})$. That is, $\boldsymbol{T}|_{\partial_{\mathrm{s}}\Omega}$ is included in the stress-like variable $\boldsymbol{q}$. Hence, without risk of confusion, the $+$ sign indicating the right hand side limit is omitted, i.e. $\bar{\boldsymbol{T}} := \bar{\boldsymbol{T}}^+$.

Remark 4. *The inelastic displacements $\boldsymbol{J}$ can be of plastic nature or damage-induced. That is, the constitutive framework presented holds also for a broad range of damage type models. If damage accumulation is to be modeled, one part of the inelastic strains has to be connected to the elastic material properties, cf. [53, 54].*

4 NUMERICAL IMPLEMENTATION

This section contains the numerical implementation of the kinematics as proposed in Section 2 as well as the constitutive equations presented in Section 3. Referring to the yield function ϕ and the evolution equations, no special assumption has to be made. Hence, the finite element model as described in this section holds for a broad range of different constitutive models.

To the best knowledge of the author, with the exception of the work [36] by BORJA, all other geometrically nonlinear embedded strong discontinuity models in the sense of SIMO et al. [7, 8] such as [25, 28, 30, 31, 34, 35] are based on the static condensation technique. In contrast to this procedure, BORJA [36] proposed a finite element formulation in which the degrees of freedom characterizing the displacement discontinuity are condensed out at the material level. In the case of infinitesimal deformations, this approach was presented in [37–39]. However, the work [36] by BORJA is restricted to constant strain triangle elements. Furthermore, the displacement jump is assumed to represent a purely sliding deformation, that is, $\boldsymbol{J} = \zeta \, \boldsymbol{M}$, with $\boldsymbol{N} \cdot \boldsymbol{M} = 0$ and ζ denoting the amplitude of the displacement discontinuity. Evidently, the underlying kinematics cannot capture mode-I or mixed-mode failure. In the two-dimensional case, these kinematics result in $\dot{\boldsymbol{M}} = \boldsymbol{0}$. Consequently, the scalar ζ is the only unknown variable associated with the displacement jump. Additionally, for a purely sliding deformation in 2D, the identity

$$\frac{\bar{\boldsymbol{F}} \cdot \boldsymbol{M}}{||\bar{\boldsymbol{F}} \cdot \boldsymbol{M}||_2} = \frac{\hat{\boldsymbol{F}} \cdot \boldsymbol{M}}{||\hat{\boldsymbol{F}} \cdot \boldsymbol{M}||_2} \tag{39}$$

holds. Hence, the tangential vector which defines the direction of the displacement jump depends only on the known (in the case of displacement based finite elements) compatible deformation field $\hat{\boldsymbol{u}}$. Both simplifications, i.e. $\dot{\boldsymbol{M}} = \boldsymbol{0}$ and Equation (39), have been included in the

numerical model as proposed in [36]. However, even for a vanishing normal component of the displacement jump ($\boldsymbol{J} \cdot \boldsymbol{N} = 0$) which is a very restrictive assumption, $\dot{\boldsymbol{M}} = \boldsymbol{0}$ is not fulfilled in 3D, in general. As a consequence, the extension of the model [36] proposed by BORJA to a fully three-dimensional framework is not a straightforward task.

In this section a three-dimensional finite element formulation suitable for a broad range of different constitutive models is presented. No constraints associated with the direction of the displacement jump are assumed a priori. Arbitrary yield functions and non-associative evolution equations can be implemented consistently.

In what follows, the fundamentals concerning the novel numerical model are described firstly. For that purpose, the finite element formulation [25, 26] which represents the first published work on embedded strong discontinuities within a finite strain setting is summarized briefly. Subsequently, the new finite element formulation will be explained.

4.1 Fundamentals

The additive decomposition of the deformation gradient according to Equation (12) is formally identical to that of the well-known EAS concept [13, 27]. Hence, the implementation of most finite element models dealing with embedded strong discontinuities such as [7, 8, 25, 28, 30, 31, 34, 35] is identical to that applied in the original EAS concept. That is, the stationarity conditions of the respective two field functional

$$\int_{\Omega^{\mathrm{e}}} \mathrm{GRAD}\boldsymbol{\eta}_0 : \boldsymbol{P} \, \mathrm{d}V = \int_{\Omega^{\mathrm{e}}} \boldsymbol{B} \cdot \boldsymbol{\eta}_0 \, \mathrm{d}V + \int_{\Gamma_{\boldsymbol{P}}} \boldsymbol{T}^{*} \cdot \boldsymbol{\eta}_0 \, \mathrm{d}A \tag{40}$$

and

$$\int_{\Omega^{\mathrm{e}}} \hat{\boldsymbol{H}} : \boldsymbol{P} \, \mathrm{d}V = 0 \tag{41}$$

depending on the displacement fields $\hat{\boldsymbol{u}}$ and $[\![\boldsymbol{u}]\!]$ build the starting point of the numerical model. In Equations (40) and (41), $\boldsymbol{\eta}_0$, $\boldsymbol{B}$ and $\boldsymbol{T}^{*}$, V^{e} denote a continuous test function, body forces, prescribed traction vectors acting on the NEUMANN boundary $\Gamma_{\boldsymbol{P}}$ and the volume of the finite element e, respectively. According to the EAS concept, the compatible part of the displacement field $\hat{\boldsymbol{u}}$ and the continuous test functions $\boldsymbol{\eta}_0$ are approximated by means of the standard shape functions N_i and the nodal values $\hat{\boldsymbol{u}}_i^{\mathrm{e}}$ and $\boldsymbol{\eta}_{0\,i}^{\mathrm{e}}$, i.e.

$$\hat{\boldsymbol{u}} = \sum_{i=1}^{n_{\mathrm{node}}} \hat{\boldsymbol{u}}_i^{\mathrm{e}} \, N_i \quad \text{and} \quad \boldsymbol{\eta}_0 = \sum_{i=1}^{n_{\mathrm{node}}} \boldsymbol{\eta}_{0\,i}^{\mathrm{e}} \, N_i. \tag{42}$$

By choosing the variation $\hat{\boldsymbol{H}}$ of the enhanced displacement gradient according to [25, 26], namely

$$\hat{\boldsymbol{H}} := -\frac{1}{V^{\mathrm{e}}} \, \boldsymbol{\beta} \otimes \boldsymbol{N} + \frac{1}{A_{\mathrm{s}}} \boldsymbol{\beta} \otimes \boldsymbol{N} \, \delta_{\mathrm{s}}, \tag{43}$$

the L_2 orthogonality condition (41) is equivalent to the weak form of traction continuity

$$\frac{1}{V^{\mathrm{e}}} \int_{\Omega^{\mathrm{e}}} \boldsymbol{P} \cdot \boldsymbol{N} \, \mathrm{d}V = \frac{1}{A_{\mathrm{s}}} \int_{\partial_{\mathrm{s}}\Omega} \boldsymbol{T}_{\mathrm{s}} \, \mathrm{d}A \tag{44}$$

where V^{e}, A_{s} and $\boldsymbol{\beta}$ represent the volume of the finite element e, the volume of the localization surface, i.e. $A_{\mathrm{s}} := \int_{\partial_{\mathrm{s}}\Omega} \mathrm{d}A$, and the variations of the displacement jump $[\![\boldsymbol{u}]\!]$, respectively.

For further details, refer to [8, 15]. Since the material displacement jump $\boldsymbol{J}$ does not appear explicitly in the formulation, but the displacement jump $[\![\boldsymbol{u}]\!]$, a material law of the type $\boldsymbol{T}_{\mathrm{s}} = \boldsymbol{T}_{\mathrm{s}}([\![\boldsymbol{u}]\!])$ is frequently applied, see [34] and [26] (Appendix). The implementation of an interface law in terms of $\boldsymbol{J}$ and $\bar{\boldsymbol{T}}$ was suggested in [12]. However, the model proposed in the cited paper is based on an interface element with regularized strong discontinuities. Following the EAS concept, the solution associated with Equations (40) and (41) is computed by solving both equation simultaneously, cf. [14].

In the present paper, a different solution strategy is proposed. For the purpose of the development of the respective model, the average value of $\boldsymbol{T} = \boldsymbol{P} \cdot \boldsymbol{N}$ is introduced via

$$\mathrm{ave}(\boldsymbol{T}) := \frac{1}{V^{\mathrm{e}}} \int\limits_{\Omega^{\mathrm{e}}} \boldsymbol{P} \cdot \boldsymbol{N} \, \mathrm{d}V. \tag{45}$$

Since $\boldsymbol{T}_{\mathrm{s}} = \boldsymbol{T}_{\mathrm{s}}([\![\boldsymbol{u}]\!])$ and $[\![\boldsymbol{u}]\!]$ has been assumed spatially constant within the respective finite element, that is, $\mathrm{GRAD}\,[\![\boldsymbol{u}]\!] = \boldsymbol{0}$, the right hand side of Equation (44) simplifies to

$$\frac{1}{A_{\mathrm{s}}} \int\limits_{\partial_{\mathrm{s}}\Omega} \boldsymbol{T}_{\mathrm{s}} \, \mathrm{d}A = \boldsymbol{T}_{\mathrm{s}}. \tag{46}$$

As a consequence, Equation (44) can be rewritten as

$$\phi = ||\mathrm{ave}(\boldsymbol{T}) - \boldsymbol{T}_{\mathrm{s}}|| = 0. \tag{47}$$

For further details, refer to [21, 22]. Clearly, Equation (47) is equivalent to

$$\phi = ||\mathrm{ave}(\bar{\boldsymbol{T}}) - \bar{\boldsymbol{T}}_{\mathrm{s}}|| = 0 \tag{48}$$

depending on vectors defined on the intermediate configuration. According to Subsection 3.2, this equation results in

$$\phi(\mathrm{ave}(\bar{\boldsymbol{T}}), \boldsymbol{q}) \leq 0. \tag{49}$$

In the case of constant strain elements, i.e. $\mathrm{GRAD}\hat{\boldsymbol{u}} = \mathrm{const}$ (with respect to $\boldsymbol{X}$), which will be considered in Subsections 4.2– 4.4, $\mathrm{GRAD}\varphi = \mathrm{const}$, and consequently, $\bar{\boldsymbol{F}} = \mathrm{const}$. Hence, $\bar{\boldsymbol{C}} = \mathrm{const}$ and $\boldsymbol{S} = \mathrm{const}$ as well, leading to $\bar{\boldsymbol{T}} = \mathrm{const}$. That is, $\mathrm{ave}(\bar{\boldsymbol{T}}) = \bar{\boldsymbol{T}}$ and the weak form of traction continuity is equivalent to the strong form

$$\phi(\bar{\boldsymbol{T}}, \boldsymbol{q}) \leq 0. \tag{50}$$

As a consequence, in the case of loading ($\lambda > 0$), the stationarity conditions (40) and (41) are equivalent to the set of equations

$$\begin{aligned} \int\limits_{\Omega^{\mathrm{e}}} \mathrm{GRAD}\boldsymbol{\eta}_0 : \boldsymbol{P} \, \mathrm{d}V &= \int\limits_{\Omega^{\mathrm{e}}} \boldsymbol{B} \cdot \boldsymbol{\eta}_0 \, \mathrm{d}V + \int\limits_{\Gamma_{\boldsymbol{P}}} \boldsymbol{T}^* \cdot \boldsymbol{\eta}_0 \, \mathrm{d}A \\ \phi(\bar{\boldsymbol{T}}, \boldsymbol{q}) &= 0. \end{aligned} \tag{51}$$

The extensions necessary for the more general case, i.e. non constant strain elements, are discussed in Subsection 4.5.

Evidently, Equations (51) show the structure of standard (local) finite element models for finite strain plasticity theory. Thus, according to computational plasticity [40, 41], the problem defined by means of Equations (51) is solved in two steps. At first, if inelastic loading is signaled, the condition of traction continuity $(51)_2$ is solved (for fixed $\hat{\boldsymbol{u}}$). Subsequently, the

solution of Equation $(51)_1$ is computed. It should be noted that despite the procedure described is not standard in finite element formulations based on the EAS concept, a similar strategy, that is a staggered solution scheme, has been successfully applied before, cf. [27]. However, with the exception that one of the algorithms proposed in [27] is based on a staggered solution scheme as well, the numerical implementation presented in this paper differs significantly from that in the just cited work.

4.2 Elastic unloading

At first, the solution associated with an elastic load step is computed. That is, the inequality $\phi(\bar{\boldsymbol{T}}, \boldsymbol{q}) < 0$ is assumed to hold within the time interval $[t_n, t_{n+1}]$ considered. Thus,

$$\boldsymbol{J}_{n+1} = \boldsymbol{J}_n, \quad \text{with} \quad (\bullet)_n := (\bullet)|_{t_n}. \tag{52}$$

Consequently, the elastic solution is computed from the weak form of equilibrium $(51)_1$ subjected to the Constraint (52). Since the left hand side of Equation $(51)_1$ does not represent the best choice for computational purposes, a standard transformation leading to

$$\int_{\Omega^e} \mathrm{GRAD}\boldsymbol{\eta}_0 : \boldsymbol{P}\, \mathrm{d}V = \int_{\Omega^e} \overline{\mathrm{grad}}\boldsymbol{\eta} : \boldsymbol{\tau}\, \mathrm{d}V, \quad \text{with} \quad \overline{\mathrm{grad}}(\bullet) := \frac{\partial(\bullet)}{\partial \boldsymbol{X}} \cdot \bar{\boldsymbol{F}}^{-1} \tag{53}$$

is applied. Hence, the solution corresponding to an elastic load step is given by the procedure

$$\begin{aligned} &\text{compute:} \quad \hat{\boldsymbol{u}}_{n+1} \quad \text{under the constraints:} \\ &\int_{\Omega^e} \overline{\mathrm{grad}}\boldsymbol{\eta} : \boldsymbol{\tau}\, \mathrm{d}V = \int_{\Omega^e} \boldsymbol{B} \cdot \boldsymbol{\eta}_0\, \mathrm{d}V + \int_{\Gamma_{\boldsymbol{P}}} \boldsymbol{T}^* \cdot \boldsymbol{\eta}_0\, \mathrm{d}A \\ &\boldsymbol{J}_{n+1} = \boldsymbol{J}_n. \end{aligned} \tag{54}$$

Analogously to standard displacement based finite element formulations, $\hat{\boldsymbol{u}}_{n+1}$ is computed by using a NEWTON type iteration. For that purpose, the interpolations $(42)_1$ resulting in

$$\overline{\mathrm{grad}}\boldsymbol{\eta} = \sum_{i=1}^{n_{\mathrm{node}}} \boldsymbol{\eta}_{0\,i}^{\mathrm{e}} \otimes \mathrm{GRAD}N_i \cdot \bar{\boldsymbol{F}}^{-1} \tag{55}$$

are inserted into Equation $(54)_1$ and the residual

$$\begin{aligned} \mathbf{R}_I = \mathop{\mathbf{A}}_{e=1}^{n_{\mathrm{ele}}} &\int_{\Omega^e} \left[\mathrm{GRAD}N_i \cdot \bar{\boldsymbol{F}}^{-1}\right] \cdot \boldsymbol{\tau}\, \mathrm{d}V \\ &- \int_{\Omega^e} N_i\, \boldsymbol{B}\, \mathrm{d}V - \int_{\Gamma^e_{\boldsymbol{P}}} N_i\, \boldsymbol{T}^*\, \mathrm{d}A \end{aligned} \tag{56}$$

is introduced. Following standard conventions in finite element methods, $\mathbf{A}$ denotes the assembly of all element contributions at the local element node i to the global residual at the global node $I \in \{1, \ldots, n_{\mathrm{gl}}\}$. According to NEWTON's method, the solution $\hat{\boldsymbol{u}}_{n+1}$ (more precisely, the increment $\Delta\hat{\boldsymbol{u}}$) associated with $\mathbf{R}_I = \mathbf{0}$ (for all global node points I) is obtained from the iterative scheme

$$\mathbf{R}_I\,|_n + \mathbf{K}^{IJ}\big|_n\ \Delta\hat{\boldsymbol{u}}_J\big|_{n+1} = \mathbf{0} \qquad \forall I = 1, \ldots, n_{\mathrm{gl}} \tag{57}$$

where $\mathbf{K}^{IJ}$ denotes the components of the global stiffness matrix, i.e.

$$\mathbf{K}^{IJ} = \frac{\partial \mathbf{R}_I}{\partial \hat{\boldsymbol{u}}_J}, \tag{58}$$

and $\hat{\boldsymbol{u}}_J$ represents the conforming part of the displacement field at global node J. Within each iteration cycle, $\hat{\boldsymbol{u}}$ is updated as $\hat{\boldsymbol{u}}_{n+1} = \hat{\boldsymbol{u}}_n + \Delta\hat{\boldsymbol{u}}_{n+1}$.

The residual $\mathbf{R}_I$ depends on the regularly distributed part of the deformation gradient. However, $\bar{\boldsymbol{F}}$ is not given explicitly. More precisely, it follows from the implicit equation

$$\bar{\boldsymbol{F}}_{n+1} = \mathbf{1} + \mathrm{GRAD}\hat{\boldsymbol{u}}_{n+1} - \bar{\boldsymbol{F}}_{n+1} \cdot \boldsymbol{J}_n \otimes \mathrm{GRAD}\varphi, \tag{59}$$

cf. Equation (13). Since Equation (59) is linear in $\bar{\boldsymbol{F}}_{n+1}$ and the tuple $(\boldsymbol{J}_n, \hat{\boldsymbol{u}}_{n+1})$ is given (in displacement based finite element formulations), the exact solution of Equation (59) yields

$$\bar{\boldsymbol{F}}_{n+1} = \mathbb{A}^{-1} : \left[\mathbf{1} + \mathrm{GRAD}\hat{\boldsymbol{u}}_{n+1}\right], \tag{60}$$

with the fourth-order tensor $\mathbb{A}$ defined as

$$\mathbb{A}_{ikpq} := \mathbb{I}_{ikpq} + \left[\mathbb{I}_{ijpq}\, J_j\, \mathrm{GRAD}\varphi_k\right]\big|_{t_n}. \tag{61}$$

Next, the components of the stiffness matrix $\mathbf{K}$ are derived. Starting with the rate form of Equation $(51)_1$, that is,

$$\int_{\Omega^e} \mathrm{GRAD}\boldsymbol{\eta}_0 : \dot{\boldsymbol{P}}\, \mathrm{d}V = \int_{\Omega^e} \dot{\boldsymbol{B}} \cdot \boldsymbol{\eta}_0\, \mathrm{d}V + \int_{\Gamma^e_{\boldsymbol{P}}} \dot{\boldsymbol{T}}^* \cdot \boldsymbol{\eta}_0\, \mathrm{d}A = 0, \tag{62}$$

together with the identity

$$\int_{\Omega^e} \mathrm{GRAD}\boldsymbol{\eta}_0 : \dot{\boldsymbol{P}}\, \mathrm{d}V = \int_{\Omega^e} \overline{\mathrm{grad}}\boldsymbol{\eta} : \left[\bar{\boldsymbol{l}} \cdot \boldsymbol{\tau} + \mathcal{L}_\nu \boldsymbol{\tau}\right]\, \mathrm{d}V \tag{63}$$

which follows from standard algebraic manipulations, the rate form of the principal of virtual work is rewritten as

$$\int_{\Omega^e} \overline{\mathrm{grad}}\boldsymbol{\eta} : \left[\bar{\boldsymbol{l}} \cdot \boldsymbol{\tau} + \mathcal{L}_\nu \boldsymbol{\tau}\right]\, \mathrm{d}V = \int_{\Omega^e} \dot{\boldsymbol{B}} \cdot \boldsymbol{\eta}_0\, \mathrm{d}V + \int_{\Gamma^e_{\boldsymbol{P}}} \dot{\boldsymbol{T}}^* \cdot \boldsymbol{\eta}_0\, \mathrm{d}A = 0. \tag{64}$$

In Equation (64), the LIE-type derivative

$$\mathcal{L}_\nu \boldsymbol{\tau} := \bar{\boldsymbol{F}} \cdot \dot{\boldsymbol{S}} \cdot \bar{\boldsymbol{F}}^T \tag{65}$$

has been introduced. Using the rate form of the hyperelastic material law (22), i.e.

$$\dot{\boldsymbol{S}} = \frac{1}{2}\, \mathbb{C} : \dot{\bar{\boldsymbol{C}}}, \quad \text{with} \quad \mathbb{C} = 4\, \frac{\partial^2 \Psi_{\mathrm{reg}}}{\partial \bar{\boldsymbol{C}} \otimes \partial \bar{\boldsymbol{C}}} \tag{66}$$

and applying the well-known identity

$$\mathcal{L}_\nu \boldsymbol{\tau} = \boldsymbol{c} : \bar{\boldsymbol{l}}, \quad \text{with} \quad c_{abcd} = \bar{F}_{aA}\, \bar{F}_{bB}\, \bar{F}_{cC}\, \bar{F}_{dD}\, \mathbb{C}_{ABCD}, \tag{67}$$

Equation (64) yields

$$\int_{\Omega^e} \overline{\mathrm{grad}}\boldsymbol{\eta} : \left[\bar{\boldsymbol{l}} \cdot \boldsymbol{\tau} + \boldsymbol{c} : \bar{\boldsymbol{l}}\right]\, \mathrm{d}V = \int_{\Omega^e} \dot{\boldsymbol{B}} \cdot \boldsymbol{\eta}_0\, \mathrm{d}V + \int_{\Gamma^e_{\boldsymbol{P}}} \dot{\boldsymbol{T}}^* \cdot \boldsymbol{\eta}_0\, \mathrm{d}A = 0. \tag{68}$$

Clearly, the only tensor in Equation (68) which depends on the rate of the conforming displacement field $\hat{\boldsymbol{u}}$ is the regularly distributed part of the spatial velocity gradient $\bar{\boldsymbol{l}}$. In the context of the iterative solution scheme according to Equation (57), $\bar{\boldsymbol{l}}$ leads to

$$\bar{\boldsymbol{l}} = \mathrm{d}\bar{\boldsymbol{F}} \cdot \bar{\boldsymbol{F}}^{-1}, \tag{69}$$

with the linearization

$$\mathrm{d}\bar{\boldsymbol{F}} = \frac{\partial \bar{\boldsymbol{F}}}{\partial \hat{\boldsymbol{u}}} \cdot \Delta\hat{\boldsymbol{u}}. \tag{70}$$

By differentiating Equation (60) for fixed $\boldsymbol{J}$ which results in

$$\mathrm{d}\bar{\boldsymbol{F}}_{n+1} = \mathbb{A}^{-1} : \mathrm{GRAD}\Delta\hat{\boldsymbol{u}}_{n+1}, \tag{71}$$

Equation (69) is rewritten as

$$\bar{\boldsymbol{l}} = \left(\mathbb{A}^{-1} : \mathrm{GRAD}\Delta\hat{\boldsymbol{u}}_{n+1}\right) \cdot \bar{\boldsymbol{F}}^{-1} \tag{72}$$

or equivalently,

$$\bar{\boldsymbol{l}} = \mathbb{L}^{\mathrm{e}} : \mathrm{GRAD}\Delta\hat{\boldsymbol{u}}_{n+1}, \quad \text{with} \quad \mathbb{L}^{\mathrm{e}}_{ijkl} = \mathbb{A}^{-1}_{ipkl}\, \bar{F}^{-1}_{pj}. \tag{73}$$

Based on Equation (73), the rate form of the principle of virtual work (68), and consequently, the stiffness matrix $\mathbf{K}^{IJ}$ can be computed. It is obtained as

$$\mathbf{K}^{IJ} = \mathbf{K}^{IJ}_{\mathrm{geo}} + \mathbf{K}^{IJ}_{\mathrm{mat}}. \tag{74}$$

In Equation (74), $\mathbf{K}^{IJ}_{\mathrm{geo}}$ denotes the so-called geometric stiffness matrix defined as

$$\mathbf{K}^{IJ}_{\mathrm{geo}} = \mathop{\mathbf{A}}_{e=1}^{n_{\mathrm{ele}}} \int_{\Omega^{\mathrm{e}}} \left[\mathrm{GRAD}N_i \cdot \bar{\boldsymbol{F}}^{-1}\right] \cdot \boldsymbol{\tau} \overset{(2)}{\cdot} \mathbb{L}^{\mathrm{e}} \cdot \mathrm{GRAD}N_j \mathrm{d}V \tag{75}$$

and $\mathbf{K}^{IJ}_{\mathrm{mat}}$ represents the material tangent. It is computed according to

$$\mathbf{K}^{IJ}_{\mathrm{mat}} = \mathop{\mathbf{A}}_{e=1}^{n_{\mathrm{ele}}} \int_{\Omega^{\mathrm{e}}} \left[\mathrm{GRAD}N_i \cdot \bar{\boldsymbol{F}}^{-1}\right] \overset{(2)}{\cdot} \boldsymbol{c} : \mathbb{L}^{\mathrm{e}} \cdot \mathrm{GRAD}N_j \mathrm{d}V. \tag{76}$$

It is obvious that now the operator $\mathbf{A}$ denotes the assembly of all element contributions ($e = 1, \ldots, n_{\mathrm{ele}}$) at the local element nodes ($i, j = 1, \ldots, n_{\mathrm{node}}$) to the components of the global stiffness matrix $\mathbf{K}^{IJ}$. Clearly, in the case of linearized kinematics, $\mathbf{K}^{IJ}_{\mathrm{geo}} = \mathbf{0}$.

4.3 Inelastic loading

Next, the solution corresponding to an inelastic loading step, i.e. $\lambda > 0$ is addressed. At first, according to the return-mapping algorithm [40, 41], a trial step characterized by purely elastic deformation is defined as

$$\begin{aligned} \lambda = 0 \quad &\Longleftrightarrow \quad \dot{\boldsymbol{J}} = \boldsymbol{0}, \quad \dot{\boldsymbol{\alpha}} = \boldsymbol{0}, \quad \dot{\boldsymbol{q}} = \boldsymbol{0} \\ &\Longrightarrow \quad \bar{\boldsymbol{F}}^{\mathrm{tr}}_{n+1} = \boldsymbol{1} + \mathrm{GRAD}\hat{\boldsymbol{u}}_{n+1} - \bar{\boldsymbol{F}}^{\mathrm{tr}}_{n+1} \cdot \boldsymbol{J}_n \otimes \mathrm{GRAD}\varphi. \end{aligned} \tag{77}$$

Clearly, $\bar{\boldsymbol{F}}^{\mathrm{tr}}_{n+1}$ is computed by applying Equation (60). With $\bar{\boldsymbol{F}}^{\mathrm{tr}}_{n+1}$ the right CAUCHY-GREEN trial tensor $\bar{\boldsymbol{C}}^{\mathrm{tr}}_{n+1}$ and the second PIOLA-KIRCHHOFF trial stresses $\boldsymbol{S}^{\mathrm{tr}}_{n+1}$ are introduced in standard manner. This leads to the trial stress vector

$$\bar{\boldsymbol{T}}^{\mathrm{tr}}_{n+1} = \bar{\boldsymbol{C}}^{\mathrm{tr}}_{n+1} \cdot \boldsymbol{S}^{\mathrm{tr}}_{n+1} \cdot \boldsymbol{N}. \tag{78}$$

As a consequence, the discrete loading condition is given as

$$\phi^{\mathrm{tr}} := \phi(\bar{\boldsymbol{T}}^{\mathrm{tr}}_{n+1}, \boldsymbol{q}^{\mathrm{tr}}_{n+1}) > 0, \quad \text{with} \quad \boldsymbol{q}^{\mathrm{tr}}_{n+1} = \boldsymbol{q}_n. \tag{79}$$

In the case $\phi^{\mathrm{tr}} \leq 0$, i.e. a purely elastic loading step, the material response is computed according to Subsection 4.2. Otherwise, if inelastic loading is signaled by $\phi^{\mathrm{tr}} > 0$, a return-mapping algorithm is performed, cf. [40, 41]. That is, at first, a backward-EULER integration is applied to the evolution Equations (36). Hence, the displacement jump (more precisely, its material counterpart) and the internal displacement-like variable $\boldsymbol{\alpha}$ at time t_{n+1} are computed as

$$\boldsymbol{J}_{n+1} = \boldsymbol{J}_n + \Delta\lambda_{n+1}\, \partial_{\bar{\boldsymbol{T}}} g|_{n+1}, \quad \boldsymbol{\alpha}_{n+1} = \boldsymbol{\alpha}_n + \Delta\lambda_{n+1}\, \partial_{\boldsymbol{q}} h|_{n+1}, \tag{80}$$

with $\Delta\lambda_{n+1} := \lambda_{n+1}\ (t_{n+1} - t_n)$. Evidently, by using a backward-EULER integration, the differential equations characterizing the solution of an inelastic load step are transformed into a nonlinear set of algebraic equation. This is solved by means of NEWTON's method. For that purpose, the residuals

$$\boldsymbol{R} := \left\{ \begin{array}{c} \boldsymbol{R}^{\boldsymbol{J}} \\ \boldsymbol{R}^{\boldsymbol{\alpha}} \end{array} \right\} := \left\{ \begin{array}{c} -\boldsymbol{J}_{n+1} + \boldsymbol{J}_n + \Delta\lambda_{n+1}\, \partial_{\bar{\boldsymbol{T}}} g|_{n+1} \\ -\boldsymbol{\alpha}_{n+1} + \boldsymbol{\alpha}_n + \Delta\lambda_{n+1}\, \partial_{\boldsymbol{q}} h|_{n+1} \end{array} \right\} \tag{81}$$

are introduced. As a consequence, the solution associated with an inelastic load step is computed from the algebraic problem

$$\boldsymbol{R} = 0 \quad \wedge \quad \phi_{n+1} = 0. \tag{82}$$

According to NEWTON's method, the linearizations of Equations (82) are required. After some algebraic manipulations, they result in

$$\mathrm{d}\boldsymbol{R} = \boldsymbol{A}^{-1}\, \boldsymbol{\Delta} + \mathrm{d}\Delta\lambda_{n+1}\, \boldsymbol{\nabla} M, \qquad \mathrm{d}\phi = \boldsymbol{\nabla}\phi \cdot \boldsymbol{\Delta} \tag{83}$$

where the notations

$$\boldsymbol{A}^{-1} := \left[\begin{array}{cc} \boldsymbol{A}^{\boldsymbol{J}\,-1} + \Delta\lambda\, \partial^2_{\bar{\boldsymbol{T}}\otimes\bar{\boldsymbol{T}}} g & \Delta\lambda_{n+1}\, \partial^2_{\bar{\boldsymbol{T}}\otimes\boldsymbol{q}} g \\ \Delta\lambda\, \partial^2_{\boldsymbol{q}\otimes\bar{\boldsymbol{T}}} h & \boldsymbol{D}^{-1} + \Delta\lambda \partial^2_{\boldsymbol{q}\otimes\boldsymbol{q}} h \end{array} \right]\Big|_{n+1}, \quad \boldsymbol{D} := -\frac{\partial \boldsymbol{q}}{\partial \boldsymbol{\alpha}} \tag{84}$$

and

$$\boldsymbol{\Delta}^T := \left[\mathrm{d}\bar{\boldsymbol{T}}; \mathrm{d}\boldsymbol{q}\right]\big|_{n+1}, \quad \boldsymbol{\nabla} M^T := \left[\partial_{\bar{\boldsymbol{T}}} g; \partial_{\boldsymbol{q}} h\right]\big|_{n+1}, \quad \boldsymbol{\nabla}\phi^T := \left[\partial_{\bar{\boldsymbol{T}}}\phi; \partial_{\boldsymbol{q}}\phi\right]\big|_{n+1} \tag{85}$$

have been used. The second-order tensor $\boldsymbol{A}^{\boldsymbol{J}}$ connects the rate of the material displacement jump $\boldsymbol{J}$ to the rate of the traction vector $\bar{\boldsymbol{T}}$ for a fixed compatible displacement field $\hat{\boldsymbol{u}}$. The identity $\mathrm{d}\bar{\boldsymbol{T}} = -\boldsymbol{A}^J \cdot \mathrm{d}\boldsymbol{J}$ is derived in Appendix A.

Based on Equations (82) and (83), the increment of the plastic multiplier during an iteration cycle is computed in matrix notation as

$$\mathrm{d}\Delta\lambda_{n+1} = \frac{\phi_{n+1} - \boldsymbol{\nabla}\phi^T\, \boldsymbol{A}\, \boldsymbol{R}}{\boldsymbol{\nabla}\phi^T \boldsymbol{A}\, \boldsymbol{\nabla} M} \quad \Rightarrow \quad \Delta\lambda_{n+1} = \Delta\lambda_n + \mathrm{d}\Delta\lambda_{n+1}. \tag{86}$$

Note that the updated deformation gradient $\bar{\boldsymbol{F}}$ ($\Delta\hat{\boldsymbol{u}} = \boldsymbol{0}$ during an iteration cycle) follows from Equation (60).

Remark 5. *According to Equation (83), the linearizations have been computed with respect to $\bar{\boldsymbol{T}}$, $\boldsymbol{q}$ and $\Delta\lambda$. Clearly, instead of choosing $\bar{\boldsymbol{T}}$ as an independent variable, the* MANDEL*-type stresses $\bar{\boldsymbol{C}} \cdot \boldsymbol{S}$ may be used. That way, the proposed return-mapping algorithm becomes formally identical to that of classical multiplicative plasticity theory. However, in this case, the dimension of the residuals increases from $\dim \bar{\boldsymbol{T}} + \dim \boldsymbol{q} + \dim \Delta\lambda = n + 4$ to $\dim(\bar{\boldsymbol{C}} \cdot \boldsymbol{S}) + \dim \boldsymbol{q} + \dim \Delta\lambda = 10 + n$. Particularly, for isotropic softening ($\dim q = 1$) which is considered in the numerical example presented in Section 5, the number of algebraic equations increase by more than a factor of 2. As a consequence, this alternative formulation has not been chosen.*

4.4 Linearization

This subsection contains the consistent linearization of the algorithm necessary for an asymptotically quadratic convergence, cf. [40]. For fully elastic unloading, this linearization has been given in Subsection 4.2. Next, attention is restricted to an inelastic loading step, i.e. $\lambda > 0$.

By applying the return-mapping algorithm as proposed in Subsection 4.3, the regularly distributed part of the deformation gradient $\bar{\boldsymbol{F}}$, the stresses $\boldsymbol{\tau}$ or $\boldsymbol{S}$ and the elastic moduli $\boldsymbol{c}$ (see Equation (67)) are computed. That is, with the exception of the spatial velocity gradient $\bar{\boldsymbol{l}}$, all variables appearing in the rate form of equilibrium (68) are known. More precisely, only the fourth-order tensor $\mathbb{L}^{\mathrm{e}}$ which is necessary for the computation of the stiffness matrices (75) and (76) has to be derived. All other variables involved in Equations (75) and (76) are well defined. Since now attention is restricted to an inelastic loading step, the fourth-oder tensor $\mathbb{L}^{\mathrm{e}}$ is renamed as $\mathbb{L}^{\mathrm{i}}$.

According to Equation (59), the linearization of the regularly distributed part of the deformation gradient yields

$$\mathrm{d}\bar{\boldsymbol{F}} = \mathrm{GRAD}\Delta\hat{\boldsymbol{u}} - \mathrm{d}\bar{\boldsymbol{F}} \cdot \boldsymbol{J} \otimes \mathrm{GRAD}\varphi - \bar{\boldsymbol{F}} \cdot \mathrm{d}\boldsymbol{J} \otimes \mathrm{GRAD}\varphi. \tag{87}$$

Consequently, $\mathrm{d}\bar{\boldsymbol{F}}$ is obtained as

$$\begin{aligned} \mathrm{d}\bar{\boldsymbol{F}} &= \mathrm{d}\bar{\boldsymbol{F}}\big|_{\boldsymbol{J}=\mathrm{const}} + \mathrm{d}\bar{\boldsymbol{F}}\big|_{\hat{\boldsymbol{u}}=\mathrm{const}} \\ &= \mathbb{A}^{-1} : \left[\mathrm{GRAD}\Delta\hat{\boldsymbol{u}} - \bar{\boldsymbol{F}} \cdot \mathrm{d}\boldsymbol{J} \otimes \mathrm{GRAD}\varphi\right]. \end{aligned} \tag{88}$$

Clearly, $\mathrm{d}\bar{\boldsymbol{F}}|_{\boldsymbol{J}=\mathrm{const}}$ represents the linearization associated with a fully elastic load step, cf. Subsection 4.2. However, the linearization $\mathrm{d}\boldsymbol{J}$ defining $\mathrm{d}\bar{\boldsymbol{F}}|_{\hat{\boldsymbol{u}}=\mathrm{const}}$ is unknown so far. It follows from the return-mapping algorithm.

At a converged state of the return-mapping algorithm, characterized by $\boldsymbol{R} = \boldsymbol{0}$ and $\phi = 0$ (cf. Subsection 4.3) the linearization of $\boldsymbol{J}$ with respect to $\bar{\boldsymbol{T}}$, $\boldsymbol{q}$ and $\Delta\lambda$ results from $\mathrm{d}\boldsymbol{R} = \boldsymbol{0}$ (see Equation (83)). Evidently, the goal of this paragraph is to linearize $\boldsymbol{J}$ with respect to the primary variable $\hat{\boldsymbol{u}}$. For that purpose, the standard procedure known from computational plasticity theory is borrowed, cf. [40, 41].

By applying the chain rule

$$\mathrm{d}\bar{\boldsymbol{T}} = \frac{\partial \bar{\boldsymbol{T}}}{\partial \bar{\boldsymbol{C}}} : \frac{\partial \bar{\boldsymbol{C}}}{\partial \bar{\boldsymbol{F}}} : \left[\mathrm{d}\bar{\boldsymbol{F}}\big|_{\boldsymbol{J}=\mathrm{const}} + \mathrm{d}\bar{\boldsymbol{F}}\big|_{\hat{\boldsymbol{u}}=\mathrm{const}}\right] \tag{89}$$

and inserting the linearization of $\boldsymbol{J}$ with respect to $\bar{\boldsymbol{T}}$, $\boldsymbol{q}$ and $\Delta\lambda$, together with $\mathcal{A}^{\boldsymbol{C}} := \partial\bar{\boldsymbol{T}}/\partial\bar{\boldsymbol{C}}$, $\mathbb{T} := \partial\bar{\boldsymbol{C}}/\partial\bar{\boldsymbol{F}}$ and $\boldsymbol{A}^{\boldsymbol{J}} := -\partial\bar{\boldsymbol{T}}/\partial\boldsymbol{J}$ according to Appendix A, Equation (89) is rewritten as

$$\begin{aligned} \mathrm{d}\bar{\boldsymbol{T}} &= \mathcal{A}^{\boldsymbol{C}} : \mathbb{T} : \mathbb{A}^{-1} : \mathrm{GRAD}\Delta\hat{\boldsymbol{u}} - \boldsymbol{A}^{\boldsymbol{J}} \cdot \mathrm{d}\boldsymbol{J} \\ &= \mathcal{A}^{\boldsymbol{C}} : \mathbb{T} : \mathbb{A}^{-1} : \mathrm{GRAD}\Delta\hat{\boldsymbol{u}} - \boldsymbol{A}^{\boldsymbol{J}} \cdot \Big[\mathrm{d}\Delta\lambda\, \partial_{\bar{\boldsymbol{T}}} g + \Delta\lambda\, \partial^2_{\bar{\boldsymbol{T}}\otimes\bar{\boldsymbol{T}}} g : \mathrm{d}\bar{\boldsymbol{T}} \\ &\quad + \Delta\lambda\, \partial^2_{\bar{\boldsymbol{T}}\otimes\boldsymbol{q}} g : \mathrm{d}\boldsymbol{q}\Big]. \end{aligned} \tag{90}$$

With the matrix $\boldsymbol{A}$ according to Equation (84), the increment of the stress vector $\bar{\boldsymbol{T}}$ and that of the internal variables $\boldsymbol{q}$ are rewritten in matrix notation as

$$\boldsymbol{A}^{-1}\,\boldsymbol{\Delta} = \begin{bmatrix} \boldsymbol{A}^{\boldsymbol{J}^{-1}} \cdot \mathcal{A}^{\boldsymbol{C}} : \mathbb{T} : \mathrm{GRAD}\Delta\hat{\boldsymbol{u}} \\ 0 \end{bmatrix} - \mathrm{d}\Delta\lambda\, \boldsymbol{\nabla} M. \tag{91}$$

Pre-multiplying Equation (91) by $\boldsymbol{\nabla}\phi^T\ \boldsymbol{A}$ and considering $\mathrm{d}\phi = \boldsymbol{\nabla}\phi^T\ \boldsymbol{\Delta} = 0$, the linearization of the plastic multiplier with respect to the primary variable $\hat{\boldsymbol{u}}$ is obtained as

$$\begin{aligned} \mathrm{d}\Delta\lambda &= \frac{\boldsymbol{\nabla}\phi^T\ \boldsymbol{A}\ \begin{bmatrix} \boldsymbol{A}^{\boldsymbol{J}^{-1}} \cdot \mathcal{A}^{\boldsymbol{C}} : \mathbb{T} : \mathrm{GRAD}\Delta\hat{\boldsymbol{u}} \\ 0 \end{bmatrix}}{\boldsymbol{\nabla}\phi^T\ \boldsymbol{A}\ \boldsymbol{\nabla}M} \\ &= \frac{\left[\partial_{\bar{\boldsymbol{T}}}\phi \cdot \boldsymbol{A}_{[11]} + \partial_{\boldsymbol{q}}\phi \cdot \boldsymbol{A}_{[21]}\right] \cdot \boldsymbol{A}^{\boldsymbol{J}^{-1}} \cdot \mathcal{A}^{\boldsymbol{C}} : \mathbb{T}}{\boldsymbol{\nabla}\phi^T\ \boldsymbol{A}\ \boldsymbol{\nabla}M} : \mathrm{GRAD}\Delta\hat{\boldsymbol{u}} \end{aligned} \tag{92}$$

where $\boldsymbol{A}_{[ij]}$ denotes the submatrix ij of the hypermatrix $\boldsymbol{A}$. Clearly, this equation is formally identical to that of the standard return-mapping algorithm, cf. [40, 41].

Next, the linearizations of $\bar{\boldsymbol{T}}$ and $\boldsymbol{q}$ with respect to the primary variable $\hat{\boldsymbol{u}}$ are computed. By inserting Equation (92) into Equation (91) and pre-multiplying Equation (91) by $\boldsymbol{A}$, these linearizations are given as

$$\begin{aligned} \mathrm{d}\bar{\boldsymbol{T}} &= \boldsymbol{A}_{[11]} \cdot \boldsymbol{A}^{\boldsymbol{J}^{-1}} \cdot \mathcal{A}^{\boldsymbol{C}} : \mathbb{T} : \mathrm{GRAD}\Delta\hat{\boldsymbol{u}} \\ &\quad - \frac{\left[\partial_{\bar{\boldsymbol{T}}}\phi \cdot \boldsymbol{A}_{[11]} + \partial_{\boldsymbol{q}}\phi \cdot \boldsymbol{A}_{[21]}\right] \cdot \boldsymbol{A}^{\boldsymbol{J}^{-1}} \cdot \mathcal{A}^{\boldsymbol{C}} : \mathbb{T}}{\boldsymbol{\nabla}\phi^T\ \boldsymbol{A}\ \boldsymbol{\nabla}M} : \mathrm{GRAD}\Delta\hat{\boldsymbol{u}}\ \partial_{\bar{\boldsymbol{T}}} g \end{aligned} \tag{93}$$

and

$$\begin{aligned} \mathrm{d}\boldsymbol{q} &= \boldsymbol{A}_{[21]} \cdot \boldsymbol{A}^{\boldsymbol{J}^{-1}} \cdot \mathcal{A}^{\boldsymbol{C}} : \mathbb{T} : \mathrm{GRAD}\Delta\hat{\boldsymbol{u}} \\ &\quad - \frac{\left[\partial_{\bar{\boldsymbol{T}}}\phi \cdot \boldsymbol{A}_{[11]} + \partial_{\boldsymbol{q}}\phi \cdot \boldsymbol{A}_{[21]}\right] \cdot \boldsymbol{A}^{\boldsymbol{J}^{-1}} \cdot \mathcal{A}^{\boldsymbol{C}} : \mathbb{T}}{\boldsymbol{\nabla}\phi^T\ \boldsymbol{A}\ \boldsymbol{\nabla}M} : \mathrm{GRAD}\Delta\hat{\boldsymbol{u}}\ \partial_{\boldsymbol{q}} h. \end{aligned} \tag{94}$$

Finally, the linearization of $\boldsymbol{J}$ with respect to the primary variable $\hat{\boldsymbol{u}}$ is obtained by inserting Equations (92)-(94) into

$$\mathrm{d}\boldsymbol{J} = \mathrm{d}\Delta\lambda\ \partial_{\bar{\boldsymbol{T}}} g + \Delta\lambda\ \partial^2_{\bar{\boldsymbol{T}}\otimes\bar{\boldsymbol{T}}} g \cdot \mathrm{d}\bar{\boldsymbol{T}} + \Delta\lambda\ \partial^2_{\bar{\boldsymbol{T}}\otimes\boldsymbol{q}} g \cdot \mathrm{d}\boldsymbol{q}. \tag{95}$$

This leads to

$$\mathrm{d}\boldsymbol{J} = \mathcal{J} : \mathrm{GRAD}\Delta\hat{\boldsymbol{u}}. \tag{96}$$

The third-oder tensor $\mathcal{J}$ is given in the Appendix B.

Now, the linearization of $\bar{\boldsymbol{F}}$ can be computed. With Equation (96), Equation (88) is rewritten as

$$\mathrm{d}\bar{\boldsymbol{F}} = \underbrace{\left[\mathbb{A}^{-1} - \left(\mathbb{A}^{-1} \cdot \mathrm{GRAD}\varphi\right) \cdot \bar{\boldsymbol{F}} \cdot \mathcal{J}\right]}_{=:\ \mathbb{P}} : \mathrm{GRAD}\Delta\hat{\boldsymbol{u}}. \tag{97}$$

Hence, $\mathbb{L}^{\mathrm{i}}$ is obtained as

$$\bar{\boldsymbol{l}} = \mathbb{L}^{\mathrm{i}} : \mathrm{GRAD}\Delta\hat{\boldsymbol{u}}_{n+1}, \quad \text{with} \quad \mathbb{L}^{\mathrm{i}}_{ijkl} = \mathbb{P}_{ipkl}\ \bar{F}^{-1}_{pj}, \tag{98}$$

cf. Equation (73). As a consequence, the geometric stiffness matrix results in

$$\mathsf{K}^{IJ}_{\mathrm{geo}} = \operatorname*{\mathsf{A}}_{e=1}^{n_{\mathrm{ele}}} \int_{\Omega^{\mathrm{e}}} \left[\mathrm{GRAD}N_i \cdot \bar{\boldsymbol{F}}^{-1}\right] \cdot \boldsymbol{\tau} \overset{(2)}{\cdot} \mathbb{L}^{\mathrm{i}} \cdot \mathrm{GRAD}N_j \mathrm{d}V \tag{99}$$

and the material tangent is given as

$$\mathsf{K}^{IJ}_{\mathrm{mat}} = \operatorname*{\mathsf{A}}_{e=1}^{n_{\mathrm{ele}}} \int_{\Omega^{\mathrm{e}}} \left[\mathrm{GRAD}N_i \cdot \bar{\boldsymbol{F}}^{-1}\right] \overset{(2)}{\cdot} \boldsymbol{c} : \mathbb{L}^{\mathrm{i}} \cdot \mathrm{GRAD}N_j \mathrm{d}V \tag{100}$$

(compare Equations (99) and (100) to Equations (75) and (76)).

Remark 6. *In the case of a constant direction of the material displacement jump, that is, an evolution equation of the type*

$$\dot{\boldsymbol{J}} = \lambda\, \boldsymbol{M}, \quad \textit{with} \quad \dot{\boldsymbol{M}} = \boldsymbol{0}, \tag{101}$$

together with an isotropic softening response, the algorithmic formulation presented can be significantly simplified, cf. Appendix C.

4.5 Extension to higher order elements

In Subsections 4.2– 4.4, the numerical implementation associated with constant strain elements has been presented. Now, the more general case is discussed. However, since the extensions necessary for higher order elements are relatively straightforward, the respective modifications of the algorithm are described in a brief manner. In the case of linearized kinematics, more details can be found in [22].

According to Subsection 4.1, for non constant strain elements, the restriction imposed by the weak form of traction continuity across $\partial_{\text{s}}\Omega$ reads

$$\phi(\text{ave}(\bar{\boldsymbol{T}}), \boldsymbol{q}) \leq 0. \tag{102}$$

Following the arguments as presented in Subsection 3.2, the evolution equations corresponding to the traction-separation law are obtained as

$$\begin{array}{rcl} \dot{\boldsymbol{J}} & = & \lambda\, \partial_{\text{ave}(\bar{\boldsymbol{T}})} g \\ \dot{\boldsymbol{\alpha}} & = & \lambda\, \partial_{\boldsymbol{q}} h. \end{array} \tag{103}$$

Analogously to the yield function, the two potentials $g(\text{ave}(\bar{\boldsymbol{T}}), \boldsymbol{q})$ and $h(\text{ave}(\bar{\boldsymbol{T}}), \boldsymbol{q})$ depend now on the average stress vector $\text{ave}(\bar{\boldsymbol{T}})$, see [22]. Clearly, the identity

$$\text{ave}(\bar{\boldsymbol{T}}) = \text{ave}(\bar{\boldsymbol{C}} \cdot \boldsymbol{S}) \cdot \boldsymbol{N} \tag{104}$$

holds.

Next, the modifications of the kinematics necessary for higher order elements are explained. All finite element formulations based on the strong discontinuity approach are based on the assumption $\partial \left[\!\left[\boldsymbol{u}\right]\!\right] / \partial \boldsymbol{X} = \boldsymbol{0}$, cf. [8, 15, 25, 31, 37, 55–57]. This condition is enforced for higher order elements as well. Clearly, instead of describing the kinematics in terms of $\left[\!\left[\boldsymbol{u}\right]\!\right]$ one can alternatively use its material counterpart $\boldsymbol{J}$. In this case, it is canonical to enforce the equivalent constraint $\partial \boldsymbol{J} / \partial \boldsymbol{X} = \boldsymbol{0}$. Combining these assumptions and computing the push forward of $\boldsymbol{J}$ in an average form, results in the transformation

$$\left[\!\left[\boldsymbol{u}\right]\!\right] = \text{ave}(\bar{\boldsymbol{F}}) \cdot \boldsymbol{J}. \tag{105}$$

A similar argument leading to Equation (105) was recently proposed by CALLARI & ARMERO [35]. Using Equation (105), the trial state of the deformation gradient at time t_{n+1} is computed as

$$\bar{\boldsymbol{F}}^{\text{tr}}_{n+1} = \boldsymbol{1} + \text{GRAD}\hat{\boldsymbol{u}}_{n+1} - \underbrace{\text{ave}\left(\bar{\boldsymbol{F}}^{\text{tr}}_{n+1}\right) \cdot \boldsymbol{J}_n}_{\left[\!\left[\boldsymbol{u}\right]\!\right]^{\text{tr}}_{n+1}} \otimes \text{GRAD}\varphi, \tag{106}$$

compare to Equation (59). From the average counterpart of Equation (106), the average trial deformation gradient is obtained as

$$\text{ave}(\boldsymbol{F}^{\text{tr}}_{n+1}) = \text{ave}(\mathbb{A})^{-1} : \left[\boldsymbol{1} + \text{ave}(\text{GRAD}\hat{\boldsymbol{u}}_{n+1})\right], \tag{107}$$

with ave($\mathbb{A}$) according to Equation (61) ($\hat{\boldsymbol{u}}_{n+1}$ and $\boldsymbol{J}_n$ are known). By inserting Equation (107) into Equation (106), the local trial deformation gradient can be computed. As a consequence, the local trial stresses and the discrete loading condition $\phi(\text{ave}(\bar{\boldsymbol{T}}^{\text{tr}}_{n+1}, \boldsymbol{q}_n)$ are well defined. For the considered hyperelastic material defined by Potential (23), the average MANDEL stresses are computed as

$$\text{ave}(\bar{\boldsymbol{C}} \cdot \boldsymbol{S}) = \lambda \, \frac{\text{ave}\,(J^2) - 1}{2} \, \boldsymbol{1} + \mu \, \left(\text{ave}\left(\bar{\boldsymbol{C}}\right) - \boldsymbol{1}\right). \tag{108}$$

4.5.1 Elastic unloading

Clearly, if $\phi(\text{ave}(\bar{\boldsymbol{T}}^{\text{tr}}_{n+1}, \boldsymbol{q}_n) \leq 0$, the solution corresponding to the trial state is already the final solution. In this case, the residuals $\mathbf{R}_I$ according to Equation (56) can be computed directly.

With the exception of the regularly distributed part of the spatial velocity gradient $\bar{\boldsymbol{l}}$, all other variables necessary to obtain the stiffness matrix are known, compare to Equation (68). Hence, the linearization of $\bar{\boldsymbol{F}}$ with respect to $\hat{\boldsymbol{u}}$ is required. By linearizing Equation (107) and inserting the result into the linearization of Equation (106), the final solution reads

$$\text{d}\bar{\boldsymbol{F}}_{n+1} = \text{GRAD}\Delta\hat{\boldsymbol{u}}_{n+1} - \left[\text{ave}(\mathbb{A})^{-1} : \text{ave}\left(\text{GRAD}\Delta\hat{\boldsymbol{u}}_{n+1}\right)\right] \cdot \boldsymbol{J}_n \otimes \text{GRAD}\varphi. \tag{109}$$

4.5.2 Inelastic loading

If an inelastic load step is signaled by $\phi(\text{ave}(\bar{\boldsymbol{T}}^{\text{tr}}_{n+1}, \boldsymbol{q}_n) > 0$, a backward-EULER integration is applied to Equations (103) and the solution of the resulting nonlinear set of algebraic Equations (82) is computed by means of NEWTON's method. However, in contrast to constant strain elements, the independent variables are now ave($\bar{\boldsymbol{T}}$), $\boldsymbol{q}$, $\Delta\lambda$. Hence, all partial derivatives with respect to $\bar{\boldsymbol{T}}$ in Subsection (4.3) have to be replaced by derivatives with respect to ave($\bar{\boldsymbol{T}}$). Since the potentials g and h and the yield function ϕ are formulated in terms of ave($\bar{\boldsymbol{T}}$) (instead of the local stress vector $\bar{\boldsymbol{T}}$), these derivatives can be computed easily.

The only significant difference between the return-mapping algorithm for constant strain elements and that for higher order elements results from the linearization of the average traction vector with respect to $\boldsymbol{J}$ (instead of $\text{d}\bar{\boldsymbol{T}} = -\boldsymbol{A}^{\boldsymbol{J}} : \text{d}\boldsymbol{J}$, compare to Appendix A). However, since

$$\text{d}\left[\text{ave}(\bar{\boldsymbol{T}})\right] = \frac{1}{V^{\text{e}}} \int_{\Omega^{\text{e}}} \text{d}\left(\bar{\boldsymbol{C}} \cdot \boldsymbol{S}\right) \cdot \boldsymbol{N} \, \text{d}V, \tag{110}$$

only the local linearization $\text{d}\left(\bar{\boldsymbol{C}} \cdot \boldsymbol{S}\right)$ is required. Hence, by applying the equations presented in Appendix A, the identity

$$\text{d}\left(\bar{\boldsymbol{C}} \cdot \boldsymbol{S}\right) \cdot \boldsymbol{N} = \mathcal{A}^{\boldsymbol{C}} : \mathbb{T} : \text{d}\bar{\boldsymbol{F}}. \tag{111}$$

is derived. Unfortunately, the linearization of $\bar{\boldsymbol{F}}$ with respect to $\boldsymbol{J}$ for constant strain elements differs from that for higher order elements. However, linearizing the average counterpart of Equation (106) with respect to $\boldsymbol{J}$ (for fixed $\hat{\boldsymbol{u}}$), leads to

$$\text{d}\left[\text{ave}(\bar{\boldsymbol{F}})\right] = -\tilde{\mathcal{G}} \cdot \text{d}\boldsymbol{J}, \tag{112}$$

with

$$\tilde{\mathcal{G}} = \text{ave}(\mathbb{A})^{-1} : \tilde{\mathcal{P}}, \qquad \tilde{\mathcal{P}}_{ijk} = \text{ave}(\bar{F}_{ik}) \, \text{ave}(\text{GRAD}\varphi_j), \tag{113}$$

compare to Step 3 in Appendix A. Finally, the linearization of the local deformation gradient with respect to $\boldsymbol{J}$ is obtained as

$$\mathrm{d}\bar{\boldsymbol{F}} = \left(\tilde{\mathcal{G}} \cdot \mathrm{d}\boldsymbol{J}\right) \cdot \boldsymbol{J} \otimes \mathrm{GRAD}\varphi - \mathrm{ave}(\bar{\boldsymbol{F}}) \cdot \mathrm{d}\boldsymbol{J} \otimes \mathrm{GRAD}\varphi =: \hat{\mathcal{G}} \cdot \mathrm{d}\boldsymbol{J}. \tag{114}$$

As a consequence, Equation (110) yields

$$\mathrm{d}\left[\mathrm{ave}(\bar{\boldsymbol{T}})\right] = \mathrm{ave}\left[\mathcal{A}^{\boldsymbol{C}} : \mathbb{T} : \hat{\mathcal{G}}\right] \cdot \mathrm{d}\boldsymbol{J}. \tag{115}$$

Now, all linearizations necessary for the return-mapping algorithm have been derived.

Remark 7. *The computation of the stiffness matrix for higher order elements is not presented in detail in this paper. However, all linearizations necessary for that purpose have been given in this subsection.*

Remark 8. *According to Equation (109), the linearization of a variable with respect to the conforming displacement field $\hat{\boldsymbol{u}}$ consists, in general, of two parts. One is associated with the local displacement gradient and one corresponds to its average counterpart. Hence, the resulting stiffness matrix shows a similar decomposition. For linearized kinematics, details can be found in [21, 22].*

5 NUMERICAL EXAMPLE

In this section, the applicability of the novel finite element formulation and its numerical performance are investigated. To the best knowledge of the author, two different benchmarks are most frequently used for the analysis of strong discontinuity approaches at finite strains: the uniaxial tension or compression test as studied in [25, 26, 28, 31, 36] or a mode-I type debinding problem, cf. [30, 34]. For the fully three-dimensional case, only one numerical analysis based on the SDA at finite strains has been presented in [34] so far. Both numerical examples, that is, the uniaxial tension/compression test as well as the mode-I type debinding problem are relatively simple. However, they are reasonable and meaningful for the analysis of the respective numerical model. The reasons for this are manifold. First, even in the case of the uniaxial compression or tension test, the stress field computed is inhomogeneous due to the initial imperfection set to activate localization. Thus, the localization surface $\partial_{\mathrm{s}}\Omega$ does not form at once. That is, an evolution of $\partial_{\mathrm{s}}\Omega$ during the numerical analysis can be observed. However, the most important property of these benchmarks is that the topology of the localization surface can be computed analytically. Furthermore, if an additional assumption concerning the activation of $\partial_{\mathrm{s}}\Omega$ is made, the complete structural response, i.e. the load-displacement curve, can be calculated analytically as well. Consequently, the results obtained numerically can be compared to the analytical solution. Particularly, for the uniaxial tension/compression test the analytical solution can be computed very easily. As a result, the applicability and the performance of the finite element formulation proposed will be demonstrated by means of the uniaxial tension test.

5.1 Set of material parameters I

In this subsection, the applicability of the proposed finite element formulation is investigated by means of shear band formation occurring in a steel made bar. The geometry and the material parameters are illustrated in Figure 1. The bar is subjected to a prescribed displacement field u at its face side. Other boundary conditions are chosen so that stresses occur only in one direction (uniaxial tension test).

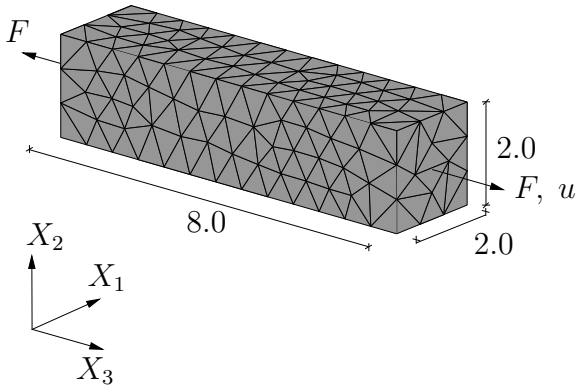

material parameters

E	= 20690	[kN/cm^2]
ν	= 0.29	
σ_{y}	= 45	[kN/cm^2]
H	= 200	[kN/cm^3]

Figure 1: Numerical study of the tension test: dimensions (in [cm]) and material parameters.

For the analysis of slip band formation in ductile materials, a VON MISES type yield function

$$\phi(\bar{\boldsymbol{T}}, q) = ||\bar{\boldsymbol{T}}_m||_2 - q(\alpha), \quad \text{with} \quad \bar{\boldsymbol{T}}_m := \bar{\boldsymbol{T}} - \left[\bar{\boldsymbol{T}} \cdot \boldsymbol{N}\right] \; \boldsymbol{N} \tag{116}$$

is adopted. That is, only the shear stresses $\bar{\boldsymbol{T}}_m$ govern the evolution of the slip sliding displacements. Following the postulate of maximum dissipation, associative evolution equations are assumed. According to Equation (116), the softening response characterized by the internal variable q is modeled as isotropic. Following [25, 26, 31], a linear evolution of q of the type

$$q(\alpha) = \sigma_{\mathrm{y}} - H \; \alpha \tag{117}$$

is chosen. In the case of linearized kinematics, the three-dimensional VON MISES type model described was proposed in [22]. In this reference, further details concerning this specific model are available.

The bulk material is modeled by applying a hyperelastic material law. The respective free energy functional is given in Equation (23). The material parameters E, ν, σ_{y} and H, used for the numerical analysis are assumed according to [26], see Figure 1.

The model is completed by a criterion necessary for the computation of the normal vector $\boldsymbol{N}$ of the localization surface. For that purpose, it assumed that the angle between the vector $\boldsymbol{N}$ and the direction of the maximum principle stress at the time of localization is about 45°. This represents a widely accepted criterion, cf. [25, 26]. In the case of linearized kinematics, it follows from a bifurcation analysis according to [7]. Clearly, the normal vector $\boldsymbol{n}$ in the deformed configuration transforms as $\boldsymbol{n} = \bar{\boldsymbol{F}}^{-1} \cdot \boldsymbol{N}$. In contrast to the localization condition proposed in [7], the shear band is assumed to propagate when the condition $\phi_{n+1} > 0$ is fulfilled (i.e. a loading step), cf. [22]. Of course, other criteria can be easily applied as well. For an overview concerning these approaches, refer to [21]. The adopted criterion shows an important advantage compared to other models. According to [22], in the case of small displacements, the load displacement curve can be computed analytically. More precisely, the maximum loading is calculated as

$$F_{\max} = 8.0 \; \sigma_y \quad \text{at} \quad u = \frac{16.0 \; \sigma_{\mathrm{y}}}{E} \tag{118}$$

and the ultimate displacement ($q = 0$, a completely softened material) as

$$u = \frac{1}{\sqrt{2}} \frac{\sigma_{\mathrm{y}}}{H}. \tag{119}$$

For further details, refer to [22].

For the assessment of mesh dependence of the results computed numerically, three different discretizations are used. The unstructured meshes II, III and IV contain 454, 1405 and

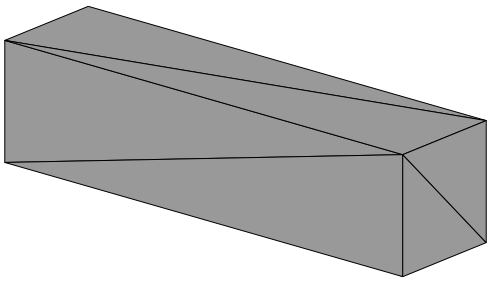

mesh I

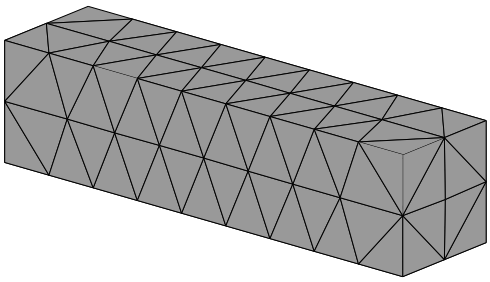

mesh II

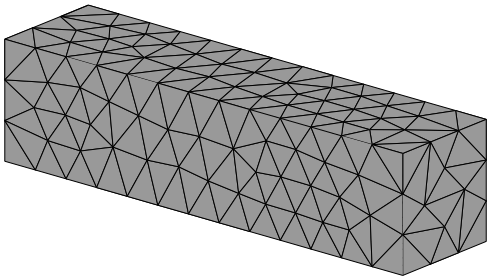

mesh III

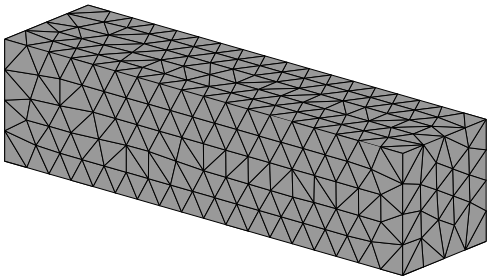

mesh IV

Figure 2: Numerical study of the tension test: finite element discretizations; mesh I, II, III and IV contain 6, 454, 1405 and 3361 constant strain tetrahedral elements.

3361 constant strain tetrahedral elements, respectively, see Figure 2. Localization is induced by slightly reducing the initial yield stress σ_{y} of one element. Since an infinite number of possible slip band orientation exists, the normal vector of the first localized element is explicitly prescribed as $\boldsymbol{N}^T = [0; 1/\sqrt{2}; 1/\sqrt{2}]$. The numerical analyses are performed with enforcing slip band path continuity. For that purpose, the following algorithm is applied: When localization is detected, the normal vector $\boldsymbol{N}$ of a new slip band is computed first. If no neighboring finite elements are localized, $\partial_{\mathrm{s}}\Omega$ is assumed to cross the centroid of the respective element. On the other side, if a slip band has already formed in one of the neighboring elements, the new band $\partial_{\mathrm{s}}\Omega$ is connected with the existing one. It should be mentioned that the discontinuous displacement field is modeled in an incompatible fashion (according to the EAS concept). Hence, the enforcement of a continuous slip band path does not guarantee that the displacement jump itself is continuous across the edge of two neighboring finite elements. For further details, refer to [22]

Additional to meshes II-IV, another discretization is considered for the sake of comparison. In contrast to the numerical analyses based on mesh II-IV, no imperfection has to be prepared for mesh I. As a result, the localization surface forms at once. Furthermore, the orientation of $\partial_{\mathrm{s}}\Omega$ is accounted for a priori. That is, opposed to the numerical analyses based on mesh II-IV, the computation performed by means of mesh I is semi numerical.

Figure 3 contains the distribution of the internal variable α representing the relative shear sliding displacement as obtained from the proposed finite element formulation. As expected, independent of the respective discretization, a mode-II failure is observed. Analogously to the analytical solution, the angle between the normal vector of the predicted shear band and that of the maximum principle stress direction is about $45°$.

The resulting load-displacement diagrams are shown in Figure 4. For the purpose of comparison, the structural response computed from the geometrically linearized model as presented in [22] is illustrated as well. As shown in Figure 4, the results obtained from the finite strain model are independent with respect to the spatial discretization. Furthermore, since the maximum displacement is relatively small ($u = 0.159099$ cm), the load-displacement diagrams

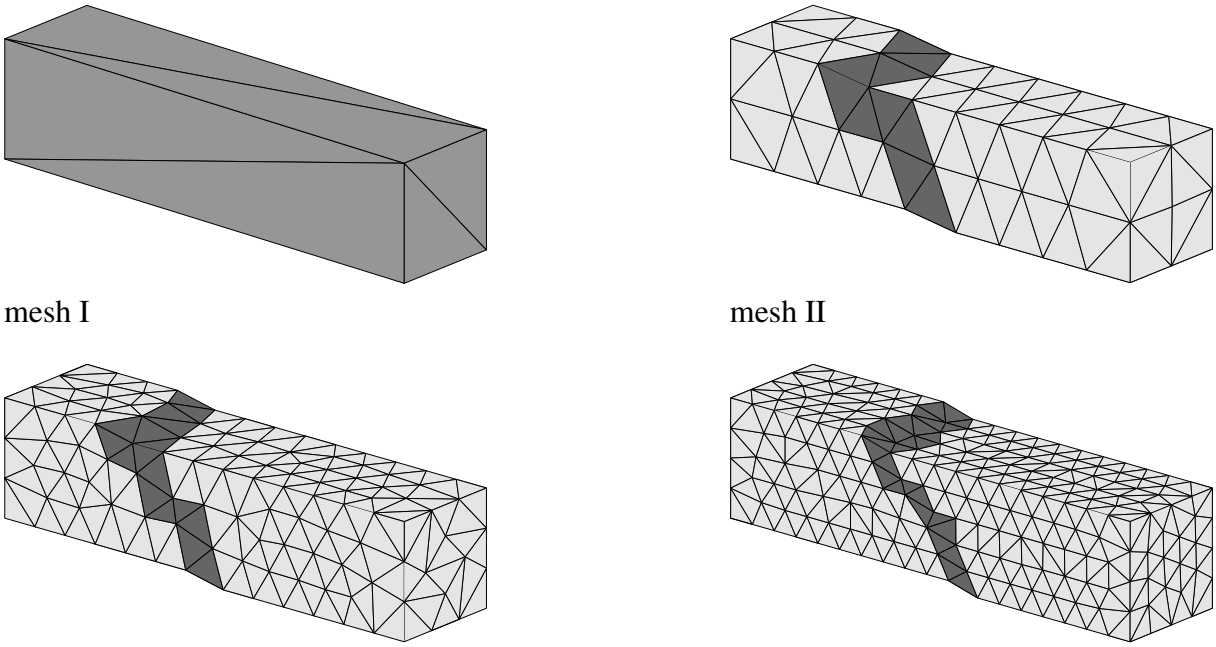

mesh I mesh II

mesh III mesh IV

Figure 3: Numerical study of the tension test: distribution of the internal variable α representing the relative shear sliding displacement as obtained from the proposed finite element formulation (1-fold magnification of the displacements); solution corresponding to the final stage of deformation ($\boldsymbol{q}(\alpha) = 0$).

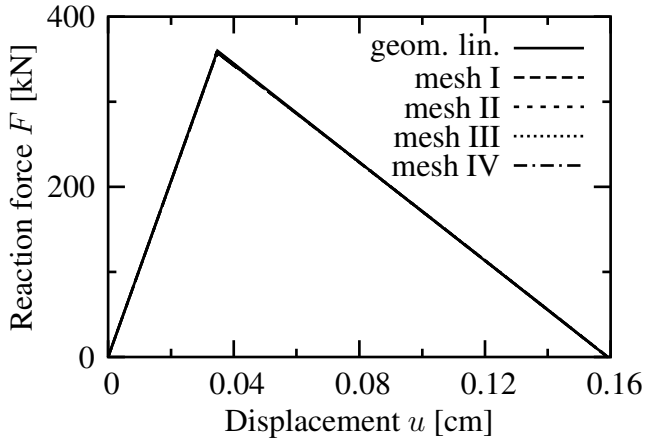

Figure 4: Numerical study of the tension test: load-displacement diagram as obtained from the proposed finite element formulation; material parameters according to Figure 1.

computed from the geometrically nonlinear model are almost identical to that predicted by the linearized finite element formulation. In summary, all results obtained numerically are identical to the small strain analytical solution as defined by means of Equations (118) and (119).

The convergence profiles for the global NEWTON type iteration are shown in Table 1. The

Iteration i	Relative error of the residuals $\mathbf{R}_I$		
	mesh II	mesh III	mesh IV
1	7.074E+00	1.561E+00	1.922E+00
2	2.041E+00	3.738E-02	2.002E-01
3	1.947E-02	4.318E-07	1.125E-05
4	1.471E-06	1.168E-12	2.594E-12
5	4.979E-12		

Table 1: Numerical study of the tension test: convergence profile of the global NEWTON type iteration; magnitude of the load step $u = 0.01$ cm; relative error of the residuals in the maximum norm; convergence tolerance for all computations $tol = 10^{-8}$.

load step considered corresponds to a displacement of the face side of $u = 0.1527$ cm. Although the prescribed increment of the nodal displacement $\Delta u = 0.01$ cm is relatively large, a rapid rate of the convergence is observed. The asymptotically quadratic convergence shows the exact linearization of the finite element formulation presented.

5.2 Set of material parameters II

In the previous subsection, the applicability as well as the efficiency of the proposed finite element model has been demonstrated. However, the material parameters which have been chosen according to [26] lead to a maximum displacement of the front size of the bar of $u = 0.159099$ cm. Hence, only relatively small strains occur and consequently, geometrical nonlinearities do not play an important role.

In this subsection, a re-analysis of the tension test as analyzed in the previous subsection is performed. In contrast to Subsection 5.1 the material parameters according to Table 2 are assumed.

E	ν	σ_{y}	H
2069 [kN/cm^2]	0.29 [-]	300 [kN/cm^2]	20 [kN/cm^3]

Table 2: Numerical study of the tension test: material parameters.

Of course, the direction of the slip band, that is, the vector $\boldsymbol{N}$ is not influenced by the change of the material parameters. Only the vector $\boldsymbol{n}$ is affected.

The computed load-displacement diagram is illustrated in Figure 5. Even before localization occurs, the elastic response as predicted from the linearized model using HOOKE's law differs from that obtained by means of the energy functional (23).

The deviation of the maximum load computed from the linearized model to that associated with the fully nonlinear algorithmic formulation is relatively large. With an ultimate load of 1891 kN (geometrically nonlinear) and 2400 kN (geometrically linearized), the relative difference follows to 27%. That is, the results obtained from the SDA model based on the assumption of small strains are clearly non conservative.

After the shear band has formed completely, a global softening response is observed. However, although a linear softening evolution of the type (117) has been adopted, a non-linear

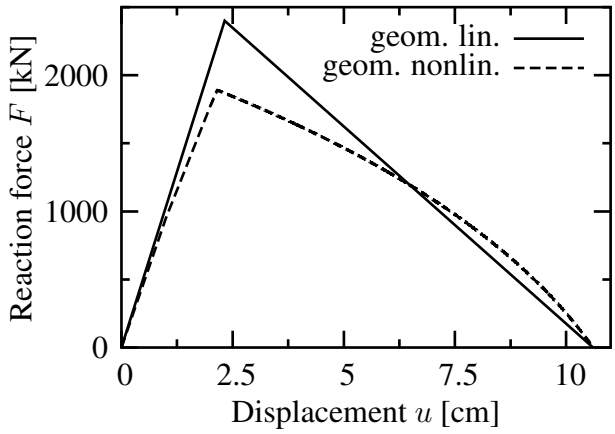

Figure 5: Numerical study of the tension test: load-displacement diagram as obtained from the proposed finite element formulation; material parameters: $E = 2.069 \cdot 10^3$ kN/cm^2, $\nu = 0.29$, $\sigma_{\mathrm{y}} = 300$ kN/cm^2, $H = 20$ kN/cm^3.

load-displacement diagram is computed. It is obvious that these nonlinearities result from the finite strain kinematics. In summary, the structural response as obtained by assuming small displacements (and strains) differs significantly from that associated with the finite strain SDA finite element formulation as presented in this paper.

It is interesting to note that the face side displacement u corresponding to a completely softened bar is independent of geometrically nonlinear kinematics. However, this is quite evident. According to Equation (117), $\alpha_{\max} = \sigma_{\mathrm{y}}/H$. Hence, at the time when the structure fails ($q = 0$), the material displacement jump $\boldsymbol{J}$ is computed as $\boldsymbol{J} = \sigma_{\mathrm{y}}/H\ [0; 1/\sqrt{2}; 1/\sqrt{2}]$. Since a stress free, completely softened bar is locally characterized by $\boldsymbol{S} = \boldsymbol{0} \iff \bar{\boldsymbol{F}} = \boldsymbol{1}$, the displacement jump $[\![\boldsymbol{u}]\!]$ is equivalent to its material counterpart $\boldsymbol{J}$, i.e. $[\![\boldsymbol{u}]\!] = \boldsymbol{J}$ (in general, $[\![\boldsymbol{u}]\!] = \bar{\boldsymbol{F}} \cdot \boldsymbol{J}$). As a consequence, the maximum displacement in the direction of the axis of the bar is computed as $[[\![\boldsymbol{u}]\!]]_3 = 1/\sqrt{2}\ \sigma_{\mathrm{y}}/H$. Clearly, this result is identical to that predicted by the geometrically linearized model.

6 CONCLUSION

An algorithmic formulation for the numerical modeling of strong discontinuities at finite strains has been presented. The proposed finite element model has been embedded into a fully three-dimensional framework. Assuming inelastic deformations to be localized, the material response has been described by means of a traction-separation law connecting the traction vector at the internal surface of strong discontinuities to the displacement jump. Referring to the yield function and the evolution equations defining the traction-separation law, no special assumption has to be made. As a consequence, the finite element formulation presented can be applied to any plasticity based interface law including isotropic and kinematic hardening, associative and non-associative evolution equations and arbitrary symmetry groups describing the anisotropic elastic or inelastic material response. Furthermore, interface laws taking stiffness degradation into account by means of damage induced displacements can be used as well.

Instead of enforcing an ad hoc traction-separation law, this law has been derived thermodynamically consistently from potentials. In the case of associative evolution equations, the interface model is defined by the space of admissible stresses and the postulate of maximum dissipation. It is interesting to note that the structure of the (discrete) cohesive material model

is formally identical to that of standard (continuous) finite strain plasticity theory. More precisely, if the dissipation is computed with respect to the intermediate configuration defined by an unloaded state (locally), this inequality is equivalent to that of nowadays classical plasticity theory. Hence, it is canonical to formulate the space of admissible stresses in terms of MANDEL stresses.

Based on the fact that the structure of the class of interface models proposed is identical to that of standard computational plasticity, an efficient algorithmic framework has been presented. Borrowing the ideas of classical computational plasticity, a return-mapping algorithm is applied. That is, in contrast to most other models based on strong discontinuities, a staggered solution strategy is employed. In the first step, the continuous displacement field is computed by assuming a fully elastic load step. Subsequently, if inelastic loading is signaled, a corrector step is computed. Analogously to the theoretical part of the paper, the presented numerical model is formally identical to that of its continuous counterpart. However, instead of defining the yield function and the evolution equations in terms of the MANDEL stress tensor, the stress vector is chosen. By this procedure, the number of unknowns is reduced leading to an increase in the efficiency.

Acknowledgement

This work was completed under the financial support of the Deutsche Forschungsgemeinschaft (DFG) through project BR 580/30-1. The author wishes to express his sincere gratitude to this support.

A Derivation of formula: $\mathrm{d}\bar{\boldsymbol{T}} = -\boldsymbol{A}^{\boldsymbol{J}} \cdot \mathrm{d}\boldsymbol{J}$; Equation (85)

The goal of this section is to derive the moduli $\boldsymbol{A}^{\boldsymbol{J}}$ connecting the material displacement jump $\boldsymbol{J}$ to the traction vector $\bar{\boldsymbol{T}}$ for a fixed conforming displacement field $\hat{\boldsymbol{u}}$. With the identity $\bar{\boldsymbol{T}} = \bar{\boldsymbol{C}} \cdot \boldsymbol{S} \cdot \boldsymbol{N}$, the linearization

$$\mathrm{d}\bar{\boldsymbol{T}} = \mathrm{d}\left(\bar{\boldsymbol{C}} \cdot \boldsymbol{S} \cdot \boldsymbol{N}\right) \tag{120}$$

is computed in three steps.

Step 1: Linearization of $\bar{\boldsymbol{T}}$ with respect to the right CAUCHY-GREEN tensor $\bar{\boldsymbol{C}}$. Applying the identity $\bar{\boldsymbol{T}} = \bar{\boldsymbol{C}} \cdot \boldsymbol{S} \cdot \boldsymbol{N}$, linearization yields

$$\begin{aligned} \mathrm{d}\left(\bar{C}_{ij}\, S_{jk}\, N_k\right) &= \underbrace{\left(\mathbb{I}^{\mathrm{sym}}_{ijpl}\, S_{jk}\, N_k + \bar{C}_{ij}\, \frac{1}{2}\, \mathbb{C}_{jkpl}\, N_k\right)}_{=:\, \mathcal{A}^{\boldsymbol{C}}_{ipl}} \mathrm{d}\bar{C}_{pl} \\ &= \left[\left(\boldsymbol{N} \cdot \boldsymbol{S} \cdot \mathbb{I}^{\mathrm{sym}} + \frac{1}{2}\, \boldsymbol{N} \overset{(2)}{\cdot} \left[\bar{\boldsymbol{C}} \cdot \mathbb{C}\right]\right) : \mathrm{d}\bar{\boldsymbol{C}}\right]_i \end{aligned} \tag{121}$$

or alternatively, in tensor notation

$$\mathrm{d}\left(\bar{\boldsymbol{C}} \cdot \boldsymbol{S} \cdot \boldsymbol{N}\right) = \mathcal{A}^{\boldsymbol{C}} : \mathrm{d}\bar{\boldsymbol{C}}. \tag{122}$$

Step 2: Linearization of $\bar{\boldsymbol{C}}$ with respect to $\bar{\boldsymbol{F}}$. Differentiating of $\bar{\boldsymbol{C}} = \bar{\boldsymbol{F}}^T \cdot \bar{\boldsymbol{F}}$ results in

$$\mathrm{d}\boldsymbol{C}_{ij} = \mathrm{d}\left(\bar{F}^T_{ik}\, \bar{F}_{kj}\right) = \underbrace{\left(\mathbb{I}_{kilp}\, \bar{F}_{kj} + \mathbb{I}_{kjlp}\, \bar{F}_{ki}\right)}_{=:\, \mathbb{T}_{ijlp}} \mathrm{d}\bar{F}_{lp} \tag{123}$$

or equivalently,

$$\mathrm{d}\bar{\boldsymbol{C}} = \mathbb{T} : \mathrm{d}\bar{\boldsymbol{F}}. \tag{124}$$

Step 3: Linearization of $\bar{\boldsymbol{F}}$ with respect to $\boldsymbol{J}$ (for fixed $\hat{\boldsymbol{u}}$). From

$$\bar{\boldsymbol{F}}_{n+1} = \boldsymbol{1} + \text{GRAD}\hat{\boldsymbol{u}}_{n+1} - \bar{\boldsymbol{F}}_{n+1} \cdot \boldsymbol{J}_{n+1} \otimes \text{GRAD}\varphi. \tag{125}$$

the identity

$$\mathrm{d}\bar{F}_{ij} = -\mathrm{d}\left(\bar{F}_{ik}\ J_k\right)\ \text{GRAD}\varphi_j = -\left(\mathbb{I}_{iklp}\ J_k\ \mathrm{d}\bar{F}_{lp} + \bar{F}_{ik}\ \mathrm{d}J_k\right)\ \text{GRAD}\varphi_j \tag{126}$$

is obtained. Equation (126) can be rewritten as

$$\underbrace{\left(\mathbb{I}_{ijlp} + \mathbb{I}_{iklp}\ J_k\ \text{GRAD}\varphi_j\right)}_{=:\ \mathbb{A}_{ijlp}}\ \mathrm{d}\bar{F}_{lp} = -\underbrace{\left(\bar{F}_{ik}\ \text{GRAD}\varphi_j\right)}_{=:\ \mathcal{P}_{ijk}}\ \mathrm{d}J_k. \tag{127}$$

Hence, finally, linearization of $\bar{\boldsymbol{F}}$ with respect to $\boldsymbol{J}$ yields

$$\mathrm{d}\bar{\boldsymbol{F}} = -\mathcal{G} \cdot \mathrm{d}\boldsymbol{J}, \tag{128}$$

with

$$\mathcal{G} = \mathbb{A}^{-1} : \mathcal{P}. \tag{129}$$

By Combining Steps 1-3, the desired linearization is computed by means of the chain rule as

$$\boldsymbol{A}^{\boldsymbol{J}} = \mathcal{A}^{\boldsymbol{C}} : \mathbb{T} : \mathcal{G}. \tag{130}$$

B Derivation of the third-order tensor $\mathcal{J}$; Equation (96)

At a converged state of the return-mapping algorithm characterized by $\boldsymbol{R} = \boldsymbol{0}$ and $\phi = 0$ (cf. Subsection 4.3), the linearization of $\boldsymbol{J}$ with respect to $\bar{\boldsymbol{T}}$, $\boldsymbol{q}$ and $\Delta\lambda$ is given as

$$\mathrm{d}\boldsymbol{J} = \mathrm{d}\Delta\lambda\ \partial_{\bar{\boldsymbol{T}}} g + \Delta\lambda\ \partial^2_{\bar{\boldsymbol{T}}\otimes\bar{\boldsymbol{T}}} g \cdot \mathrm{d}\bar{\boldsymbol{T}} + \Delta\lambda\ \partial^2_{\bar{\boldsymbol{T}}\otimes\boldsymbol{q}} g \cdot \mathrm{d}\boldsymbol{q}, \tag{131}$$

cf. Equation (83). Finally, inserting Equations (92)-(94) yields

$$\mathrm{d}\boldsymbol{J} = \mathcal{J} : \text{GRAD}\Delta\hat{\boldsymbol{u}}, \tag{132}$$

with

$$\begin{aligned}\mathcal{J} = \ & \Delta\lambda\ \left[\partial^2_{\bar{\boldsymbol{T}}\otimes\bar{\boldsymbol{T}}} g \cdot \boldsymbol{A}_{[11]} + \partial^2_{\bar{\boldsymbol{T}}\otimes\boldsymbol{q}} \cdot \boldsymbol{A}_{[21]}\right] \cdot \boldsymbol{A}^{\boldsymbol{J}^{-1}} \cdot \mathcal{A}^{\boldsymbol{C}} : \mathbb{T} \\ & - \left[\Delta\lambda\ \partial_{\bar{\boldsymbol{T}}} g \cdot \partial^2_{\bar{\boldsymbol{T}}\otimes\bar{\boldsymbol{T}}} g + \Delta\lambda\ \partial_{\boldsymbol{q}} h \cdot \partial^2_{\boldsymbol{q}\otimes\bar{\boldsymbol{T}}} g - \partial_{\bar{\boldsymbol{T}}} g\right] \\ & \otimes \left[\frac{\left[\partial_{\bar{\boldsymbol{T}}}\phi \cdot \boldsymbol{A}_{[11]} + \partial_{\boldsymbol{q}}\phi \cdot \boldsymbol{A}_{[21]}\right] \cdot \boldsymbol{A}^{\boldsymbol{J}^{-1}} \cdot \mathcal{A}^{\boldsymbol{C}} : \mathbb{T}}{\boldsymbol{\nabla}\phi^T\ \boldsymbol{A}\ \boldsymbol{\nabla} M}\right].\end{aligned} \tag{133}$$

C A simplified return-mapping algorithm for models based on a time invariant direction of the displacement jump ($\dot{\boldsymbol{M}} = \boldsymbol{0}$)

In this section, an evolution of the displacement discontinuity of the type

$$\dot{\boldsymbol{J}} = \lambda\ \boldsymbol{M}, \quad \text{with} \quad \dot{\boldsymbol{M}} = \boldsymbol{0}. \tag{134}$$

is considered. That is, the direction of the material jump $\boldsymbol{J}$ is assumed as time invariant. Furthermore, a yield function according to

$$\phi(\bar{\boldsymbol{T}}, q) \leq 0, \quad \text{with} \quad \phi = T_{\text{eq}}(\bar{\boldsymbol{T}}) - q(\alpha) \tag{135}$$

is assumed. In Equation (135), T_{eq} represents an equivalent stress measure defining the space of admissible stresses. Clearly, the assumptions (134) and (135) are very restrictive. However, for two-dimensional problems, they are reasonable in many cases. For instance, in [25, 36] the formation of slip bands is analyzed numerically by means of a SDA based finite element formulation. In these references, the respective models comply with the restrictions (134) and (135).
Since the evolution equations for $\boldsymbol{J}$ and α depend only on $\Delta\lambda$, the return-mapping algorithm reduces to a single scalar valued equation, i.e.

$$\phi(\bar{\boldsymbol{T}}_{n+1}, q_{n+1}) = 0 \quad \Rightarrow \quad \Delta\lambda_{n+1}. \tag{136}$$

For the model considered, the linearization of ϕ necessary for a NEWTON type iteration reads

$$\mathrm{d}\phi = (\partial_{\bar{\boldsymbol{T}}}\phi \otimes \boldsymbol{N}) : \frac{\partial(\bar{\boldsymbol{C}} \cdot \boldsymbol{S})}{\partial \bar{\boldsymbol{C}}} : \frac{\partial \bar{\boldsymbol{C}}}{\partial \bar{\boldsymbol{F}}} : \mathrm{d}\bar{\boldsymbol{F}} - \partial_\alpha q \ \mathrm{sign}[\mathrm{d}\Delta\lambda] \ \mathrm{d}\Delta\lambda. \tag{137}$$

By applying the identity ($\hat{\boldsymbol{u}} = \text{const}$ during the NEWTON iteration)

$$\mathrm{d}\bar{\boldsymbol{F}} = -\mathrm{d}\Delta\lambda \ \mathbb{A}^{-1} : \left(\bar{\boldsymbol{F}} \cdot \boldsymbol{M} \otimes \mathrm{GRAD}\varphi\right), \tag{138}$$

Equation (137) is rewritten as

$$\begin{aligned} \mathrm{d}\phi = -\Big[&(\partial_{\bar{\boldsymbol{T}}}\phi \otimes \boldsymbol{N}) : \frac{\partial(\bar{\boldsymbol{C}} \cdot \boldsymbol{S})}{\partial \bar{\boldsymbol{C}}} : \frac{\partial \bar{\boldsymbol{C}}}{\partial \bar{\boldsymbol{F}}} : \mathbb{A}^{-1} : \left(\bar{\boldsymbol{F}} \cdot \boldsymbol{M} \otimes \mathrm{GRAD}\varphi\right) \\ &+ \partial_\alpha q \ \mathrm{sign}[\mathrm{d}\Delta\lambda] \Big] \ \mathrm{d}\Delta\lambda =: F \ \mathrm{d}\Delta\lambda. \end{aligned} \tag{139}$$

As a consequence, the resulting iterative solution scheme is obtained as

$$\phi_n + F_n \ \mathrm{d}\Delta\lambda = 0 \quad \Rightarrow \quad \Delta\lambda_{n+1} = \Delta\lambda_n + \mathrm{d}\Delta\lambda \quad \Rightarrow \quad \boldsymbol{J}_{n+1}, \ \alpha_{n+1}. \tag{140}$$

Based on $\boldsymbol{J}_{n+1}$ the updated $\mathbb{A}^{-1}(\boldsymbol{J}_{n+1})$ and subsequently, $\bar{\boldsymbol{F}}_{n+1}$ is computed, cf. Equation (61). As a consequence, the state variables at step $n+1$ are completely known and the next iteration step can be calculated.
Next, the algorithmic tangent will be derived. For that purpose, the linearization of $\bar{\boldsymbol{F}}$ with respect to the conforming displacement field $\hat{\boldsymbol{u}}$ has to be computed, cf. Subsection 4.4 and Equation (97). At a converged state, that is, $\phi_n = 0$, the linearization of $\bar{\boldsymbol{F}}$ reads

$$\mathrm{d}\bar{\boldsymbol{F}} = \mathbb{A}^{-1} : \left[\mathrm{GRAD}\Delta\hat{\boldsymbol{u}} - \mathrm{d}\Delta\lambda \ \bar{\boldsymbol{F}} \cdot \boldsymbol{M} \otimes \mathrm{GRAD}\varphi\right]. \tag{141}$$

Inserting Equation (141) into Equation (137), the identity

$$\mathrm{d}\Delta\lambda = \frac{1}{F} \ \boldsymbol{W} : \mathrm{GRAD}\Delta\bar{\boldsymbol{u}}, \tag{142}$$

with

$$\boldsymbol{W} = (\partial_{\bar{\boldsymbol{T}}}\phi \otimes \boldsymbol{N}) : \frac{\partial(\bar{\boldsymbol{C}} \cdot \boldsymbol{S})}{\partial \bar{\boldsymbol{C}}} : \frac{\partial \bar{\boldsymbol{C}}}{\partial \bar{\boldsymbol{F}}} : \mathbb{A}^{-1} \tag{143}$$

is obtained. Finally, by combing Equation (142) with Equation (141), the desired linearization can be computed. It results in

$$\mathrm{d}\bar{\boldsymbol{F}} = \mathbb{A}^{-1} : \left[\mathbb{I} - \frac{1}{F} \ \bar{\boldsymbol{F}} \cdot \boldsymbol{M} \otimes \mathrm{GRAD}\varphi \otimes \boldsymbol{W}\right] : \mathrm{GRAD}\Delta\hat{\boldsymbol{u}}. \tag{144}$$

References

[1] R. De Borst. *Non-linear analysis of frictional materials*. PhD thesis, Technical University Delft, 1986.

[2] R. De Borst. Some recent issues in computational mechanics. *International Journal for Numerical Methods in Engineering*, 52:63–95, 2001.

[3] G. Pijaudier-Cabot and Z.P. Bažant. Nonlocal damage theory. *Journal of Engineering Mechanics (ASCE)*, 113:1512–1533, 1987.

[4] Z.P. Bažant and G. Pijaudier-Cabot. Nonlocal damage, localization, instability and convergence. *Journal of Applied Mechanics*, 55:287–293, 1988.

[5] H.B. Mühlhaus and E.C. Aifantis. A variational principle for gradient plasticity. *International Journal for Solids and Structures*, 28:845–857, 1991.

[6] R. De Borst and H.B. Mühlhaus. Gradient-dependent plasticity: Formulation and algorithmic aspects. *International Journal for Numerical Methods in Engineering*, 35:521–539, 1992.

[7] J. Simo, J. Oliver, and F. Armero. An analysis of strong discontinuities induced by strain softening in rate-independent inelastic solids. *Computational Mechanics*, 12:277–296, 1993.

[8] J. Simo and J. Oliver. A new approach to the analysis and simulation of strain softening in solids. In Z.P. Bažant, Z. Bittnar, M. Jirásek, and J. Mazars, editors, *Fracture and Damage in Quasibrittle Structures*, pages 25–39. E. &F.N. Spon, London, 1994.

[9] E.N. Dvorkin, A. M. Cuitiño, and G. Gioia. Finite elements with displacement interpolated embedded localization lines insensitive to mesh size and distortions. *International Journal for Numerical Methods in Engineering*, 30:541–564, 1990.

[10] M. Klisinski, K. Runesson, and S.. Sture. Finite element with inner softening band. *Journal of Engineering Mechanics (ASCE)*, 117(3):575–587, 1991.

[11] L.S. Lee and G.N. Pande. A new joint element for the analysis of media having discrete discontinuities. *Mechanics of Cohesive-Frictional Materials*, 4:487–504, 1999.

[12] R. Larsson and N. Jansson. Geometrically non-linear damage interface based on regularized strong discontinuities. *International Journal for Numerical Methods in Engineering*, 54:473–497, 2002.

[13] J.C. Simo and S. Rifai. A class mixed assumed strain methods and the method of incompatible modes. *International Journal for Numerical Methods in Engineering*, 29:1595–1638, 1990.

[14] J.C. Simo and F. Armero. Geometrically non-linear enhanced strain mixed methods and the method of incompatible modes. *International Journal for Numerical Methods in Engineering*, 33:1413–1449, 1992.

[15] J. Oliver. Modelling strong discontinuities in solid mechanics via strain softening constitutive equations part 1: Fundamentals. part 2: Numerical simulations. *International Journal for Numerical Methods in Engineering*, 39:3575–3623, 1996.

[16] N. Moës, J. Dolbow, and T. Belytschko. A finite element method for crack growth without remeshing. *International Journal for Numerical Methods in Engineering*, 46:131–150, 1999.

[17] J. Dolbow, N. Moës, and T. Belytschko. An extended finite element method for modeling crack growth with frictional contact. *Computer Methods in Applied Mechanics and Engineering*, submitted, 2002.

[18] J Oliver. On the discrete constituve models induced by strong discontinuity kinematics and continuum constitutive equations. *International Journal for Solids and Structures*, 37:7207 – 7229, 2000.

[19] A. Hillerborg, M. Modeer, and P.E. Petersson. Analysis of crack formation and crack growth in concrete by means of fracture mechanics and finite elements. *Cement and Concrete Research*, 6:773–782, 1976.

[20] G.I. Barenblatt. The mathematical theory of equilibrium cracks in brittle fracture. *Adv. Appl. Mech.*, 7:55–129, 1962.

[21] J. Mosler. On the modeling of highly localized deformations induced by material failure: The strong discontinuity approach. *Archives of Computational Methods in Engineering*, 11(4):389–446, 2004.

[22] J. Mosler. A novel algorithmic framework for the numerical implementation of locally embedded strong discontinuities. *Computer Methods in Applied Mechanics and Engineering*, 2004. in press.

[23] P. Steinmann, R. Larsson, and K. Runesson. On the localization properties of multiplicative hyperelasto-plastic continua with strong discontinuities. *International Journal for Solids and Structures*, 34:969–990, 1997.

[24] N.E. Jansson. *Modelling of delamination growth in composite structures*. PhD thesis, Department of Applied Mechanics, Chalmers University of Technology, 2002.

[25] F. Armero and K. Garikipati. An analysis of strong discontinuities in multiplicative finite strain plasticity and their relation with the numerical simulation of strain localization in solids. *International Journal for Solids and Structures*, 33:2863–2885, 1996.

[26] K. Garikipati. *On strong discontinuities in inelastic solids and their numerical simulation*. PhD thesis, Stanford University, 1996.

[27] J. Simo, F. Armero, and R.L. Taylor. Improved versions of assumed enhanced strain trilinear elements for 3d deformation problems. *Computer Methods in Applied Mechanics and Engineering*, 110:359–386, 1993.

[28] R. Larsson, P. Steinmann, and K. Runesson. Finite element embedded localization band for finite strain plasticity based on a regularized strong discontinuity. *Mechanics of Cohesive-Frictional Materials*, 4:171–194, 1998.

[29] P. Steinmann and P. Betsch. A localization capturing FE-interface based on regularized strong discontinuities at large inelastic strains. *International Journal for Solids and Structures*, 37:4061–4082, 2000.

[30] J. Oliver, A.E. Huespe, M.D.G. Pulido, and E. Samaniego. On the strong discontinuity approach in finite deformation settings. *International Journal for Numerical Methods in Engineering*, 56:1051–1082, 2003.

[31] F. Armero. Large-scale modeling of localized dissipative mechanisms in a local continuum: applications to the numerical simulation of strain localization in rate-dependent inelastic solids. *Mechanics of Cohesive-Frictional Materials*, 4:101–131, 1999.

[32] C. Miehe and J. Schröder. Post-critical discontinuous analysis of small-strain softening elastoplastic solids. *Archive of Applied Mechanics*, 64:267–285, 1994.

[33] U. Ohlsson and T. Olofsson. Mixed-mode fracture and anchor bolts in concrete: Analysis with inner softening bands. *Journal of Engineering Mechanics (ASCE)*, 123:1027–1033, 1997.

[34] Th.C. Gasser and G.A. Holzapfel. Geometrically non-linear and consistently linearized embedded strong discontinuity models for 3D problems with an application to the dissection analysis of soft biological tissues. *Computer Methods in Applied Mechanics and Engineering*, 192:5059–5098, 2003.

[35] C. Callari and F. Armero. Analysis and numerical simulations of straong discontinuities in finite strain poroplasticity. *Computer Methods in Applied Mechanics and Engineering*, 193:2941–2986, 2004.

[36] R.I. Borja. Finite element simulation of strain localization with large deformation: capturing strong discontinuity using a Petrov-Galerkin multiscale formulation. *Computer Methods in Applied Mechanics and Engineering*, 191:2949–2978, 2002.

[37] R.I. Borja. A finite element model for strain localization analysis of strongly discontinuous fields based on standard galerkin approximation. *Computer Methods in Applied Mechanics and Engineering*, 190:1529–1549, 2000.

[38] J. Mosler and G. Meschke. 3D FE analysis of cracks by means of the strong discontinuity approach. In E. Oñate, G. Bugeda, and B. Suárez, editors, *European Congress on Computational Methods in Applied Sciences and Engineering*, 2000.

[39] J. Mosler and G. Meschke. FE-modeling of displacement discontinuities in inelastic continua. *Zeitschrift für Angewandte Mathematik und Mechanik*, 81(Suppl. 4):875–876, 2001.

[40] J. Simo and T.J.R. Hughes. *Computational inelasticity*. Springer, New York, 1998.

[41] J.C. Simo. Numerical analysis of classical plasticity. In P.G. Ciarlet and J.J. Lions, editors, *Handbook for numerical analysis*, volume IV. Elsevier, Amsterdam, 1998.

[42] J. Mosler. *Finite Elemente mit sprungstetigen Abbildungen des Verschiebungsfeldes für numerische Analysen lokalisierter Versagenszustände in Tragwerken*. PhD thesis, Ruhr University Bochum, 2002.

[43] H. Matthies, G. Strang, and E. Christiansen. The saddle point of a differential program. In Glowinski, Robin, and Zienkiewicz, editors, *Energy methods in finite element analysis*, pages 309–318. J. Wiley and sons: London, 1979.

[44] R. Teman and G. Strang. Functions of bounded deformations. *Archive for Rational Mechanics ans Analysis*, 75:7–21, 1980.

[45] I. Stakgold. *Boundary value problems of mathematical physics*, volume I. Macmillien Series in Advanced Mathematics and theoretical physics, 1967.

[46] I. Stakgold. *Green's functions and boundary value problems*. Wiley, 1998.

[47] J. Mosler. On advanced solution strategies to overcome locking effects in strong discontinuity approaches. *International Journal for Numerical Methods in Engineering*, 2005. in press.

[48] P. Ciarlet. *Mathematical elasticity. Volume I: Three-dimensional elasticity*. North-Holland Publishing Company, Amsterdam, 1988.

[49] M. F. Snyman, W. W. Bird, and J. B. Martin. A simple formulation of a dilatant joint element governed by Coulomb friction. *Engineering Computations*, 8:215–229, 1991.

[50] F. Armero. Localized anisotropic damage of brittle materials. In D.R.J. Owen, E. Oñate, and E. Hinton, editors, *Computational Plasticity*, volume 1, pages 635–640, 1997.

[51] J. Lubliner. On the thermodynamic foundations of non-linear solid mechanics. *International Journal of Non-Linear Mechanics*, 7:237–254, 1972.

[52] J. Lubliner. *Plasticity theory*. Maxwell Macmillan International Edition, 1997.

[53] J. Mosler and O.T. Bruhns. A 3D anisotropic elastoplastic-damage model using discontinuous displacement fields. *International Journal for Numerical Methods in Engineering*, 60:923–948, 2004.

[54] J. Mosler. On the efficient implementation of an elastoplastic damage model for large-scale analyses of material failure: A multiscale approach. *Computers & Structures*, 83(4-5):369–382, 2005.

[55] M. Jirásek and T. Zimmermann. Embedded crack model: Part I: Basic formulation, Part II: Combination with smeared cracks. *International Journal for Numerical Methods in Engineering*, 50:1269–1305, 2001.

[56] R. Larrson and K. Runesson. Element-embedded localization band based on regularized displacement discontinuity. *Journal of Engineering Mechanics (ASCE)*, 122:402–411, 1996.

[57] G.N. Wells and L.J. Sluys. Three-dimensional embedded discontinuity model for brittle fracture. *International Journal for Solids and Structures*, 38:897–913, 2001.